OUKA
Osaka University Knowledge Archive

Title	POLARIZATlON AND ASYMMETRIC WEAK DECAY OF 5ΛHe
Author(s)	味村, 周平
Citation	大阪大学, 1998, 博士論文
Version Type	VoR
URL	https://doi.org/10.11501/3151109
rights	
Note	

Osaka University Knowledge Archive : OUKA

https://ir.library.osaka-u.ac.jp/

Osaka University

POLARIZATION AND ASYMMETRIC WEAK DECAY OF ${}^{5}_{\Lambda}\mathrm{He}$

SHUHEI AJIMURA

MARCH 1998

DISSERTATION IN PHYSICS

OSAKA UNIVERSITY
GRADUATE SCHOOL OF SCIENCE
TOYONAKA, OSAKA

Abstract

The weak decay of the ${}^{5}_{\Lambda}$He hypernucleus was studied by measuring an asymmetry of decay particles with respect to Λ spin polarization. The asymmetry is due to the interference between parity conserving and parity violating amplitudes of the weak decay. Hypernuclei has two decay modes, mesonic($\Lambda \rightarrow N\pi$) and nonmesonic($\Lambda N \rightarrow NN$) decay. The nonmesonic decay is the strangeness changing ΛN weak process. The asymmetry of a nonmesonic decay thus provides the information on spin-parity structure of the weak ΛN interaction, while the branching ratio ($\Gamma_{\Lambda n \rightarrow nn}/\Gamma_{\Lambda p \rightarrow np}$) provides the information on isospin structure.

${}^{5}_{\Lambda}$He was produced by the ^{6}Li$(\pi^+, K^+){}^{6}_{\Lambda}$Li reaction followed by proton emission. The (π^+, K^+) reaction introduces the polarization to ${}^{5}_{\Lambda}$He which is caused mainly by the polarization in its elementary n$(\pi^+, K^+)\Lambda$ process. In ${}^{5}_{\Lambda}$He, Λ is coupled with the ^{4}He core which has a spin-parity 0^+. The Λ polarization is explicitly same as the polarization of ${}^{5}_{\Lambda}$He. The asymmetry parameter for the mesonic decay of ${}^{5}_{\Lambda}$He is almost same as that for the free Λ decay, since the spin-parity of ${}^{5}_{\Lambda}$He $1/2^+$ is same as that of free Λ. The polarization of ${}^{5}_{\Lambda}$He was determined by measuring up/down asymmetry of the π^- mesonic decay for the first time. The obtained polarizations were $P_\Lambda = 0.25 \pm 0.08^{+0.03}_{-0.02}$, $0.39 \pm 0.09 \pm 0.02$ averaged in the regions of the scattering angle θ_K=2$\sim$7, 7$\sim$15 degrees, respectively. The polarized hypernuclei was really produced and the polarization was consistent with DWIA calculation based on the elementary amplitudes for the (π^+, K^+) reaction.

The asymmetry of protons from the nonmesonic decay of ${}^{5}_{\Lambda}$He was measured as $A_p/k = 0.11 \pm 0.08 \pm 0.01$, $0.05 \pm 0.10 \pm 0.01$ in the two scattering-angle regions. The results show the asymmetry parameter is $\alpha_p^{NM} = 0.24 \pm 0.21$ using the polarization obtained by the asymmetry of mesonic decay. ${}^{5}_{\Lambda}$He is the simplest hypernucleus in that can be studied experimentally, since the nonmesonic decay rate drops for 3- or 4-body hypernucleus drastically. All the nucleons and Λ sit in S-orbital. There is thus little ambiguity to reduce the present asymmetry parameter. Combining with the existing experimental data of the branching ratio, final isospin I_f=1 amplitudes are dominant and the phase of I_f=1 and 0 amplitudes are same. While meson exchange model predict dominance of I_f=0 amplitudes due to the strong tensor force in pion exchange potential and the phase of these amplitudes are relatively opposite to the I_f=1 amplitudes. There is no theoretical calculation agreed with the present asymmetry parameter as well as the branching ratio.

Contents

List of Tables

List of Figures

Chapter 1

Introduction

1.1 Weak decay of Λ hypernuclei

A Λ hypernucleus is a nucleus which contains a Λ hyperon inside the nuclear matter. Because of a new quantum number, "strangeness," Λ in hypernucleus is free from Pauli blocking. Thus the Λ can stay in any nuclear orbits which fact allows us to investigate the inner region of the nuclear core.

Since the Λ hyperon is a lightest particle in the baryon octet, the bound states of Λ hypernuclei are stable against decays due to the strong interaction. Their excited states decay to their ground states by electromagnetic transitions. The ground state decays only by a strangeness changing weak transition. The Λ in nuclear matter has four hadronic weak decay modes:

- Mesonic decays($\Lambda \to N + \pi$: $\Delta q \sim 100$ MeV/c)

$$\Lambda \to p + \pi^- \tag{1.1}$$

$$\Lambda \to n + \pi^0 \tag{1.2}$$

- Nonmesonic decays($\Lambda + N \to N + N$: $\Delta q \sim 400$ MeV/c)

$$\Lambda + p \to n + p \tag{1.3}$$

$$\Lambda + n \to n + n \tag{1.4}$$

Here the radiative and semi-leptonic decay modes($\Lambda \to n\gamma$, $\Lambda \to l\overline{\nu}$ or so) are not discussed since their small branching ratios, $< \sim 10^{-3}$, currently require future high intensity accelerator. The momentum transfer of the mesonic decays is about 100 MeV/c which is below the Fermi momentum of nucleons in nucleus. The mesonic decay is thus suppressed in the nuclear matter because of the Pauli blocking effect on

outgoing nucleon. Contrary, the nonmesonic decays has larger momentum transfer, about 400 MeV/c which makes the nonmesonic decay dominant for medium and heavy hypernuclei($A \geq 10$).

1.1.1 Mesonic decay

The interest of the mesonic decays is in the structure of Λ hypernucleus since the elementary process of mesonic decay is well known by the free Λ decay. For p-shell hypernuclei, the decay rate of mesonic decay has been calculated based on shell model configuration with pion distortion[1]. The calculation demonstrated the drastic changing of π^0- and π^--decay rates and their ratio depending on the hypernuclear species. For example, the proton from the π^--decay of ${}^{12}_{\Lambda}\mathrm{C}$ has to go above the $p_{3/2}$-closure, while in ${}^{12}_{\Lambda}\mathrm{B}$ the proton is allowed to occupy a hole in $p_{3/2}$ orbit. Then the π^--decay rate is more suppressed for ${}^{12}_{\Lambda}\mathrm{C}$. The calculation also demonstrated the angular distribution of pions from the polarized hypernuclei, depending on the initial and final spin states.

Recently the precise measurement of the decay rates was carried out for 4-body Λ hypernuclei(${}^{4}_{\Lambda}\mathrm{He}$, ${}^{4}_{\Lambda}\mathrm{H}$)[2]. The decay rate of mesonic decay is sensitive to the Λ wave function and is able to discriminate the Λ-nucleus potential. The decay rates agree with the calculation where a central repulsive core is introduced into the potential[3].

1.1.2 Nonmesonic decay

The strong interaction between baryons has been studied from a number of nucleon-nucleon scattering data and a few data on the hyperon-nucleon scattering with the help of $SU_F(3)$ symmetry. Contrary the weak nucleon-nucleon interaction is hard to access experimentally except for the parity violating part with very small effect compared to the strong interaction. The study of the nonmesonic decay of Λ hypernuclei gives the information on the weak hyperon-nucleon interaction. Both parity violating and parity conserving part of the interaction can be studied in the decay since no strong interaction participates such strangeness changing process. Thus the understanding of the nonmesonic decay should be the first step to investigate the weak baryon-baryon interaction.

We have two types of information from the nonmesonic decay, (1)total and partial decay rate(Γ) and (2)asymmetry parameter(α). Following descriptions are overviews of the information.

Initial state	Final state	Matrix element	Rate	Final isospin	Parity change
$^1S_0$	$^1S_0$	a	a^2	1	no
	$^1P_0$	$\frac{b}{2}(\sigma_1-\sigma_2)q$	b^2	1	yes
$^3S_1$	$^3S_1$	c	c^2	0	no
	$^3D_1$	$\frac{d}{2\sqrt{2}}S_{12}(q)$	d^2	0	no
	$^1P_1$	$\frac{\sqrt{3}}{2}e(\sigma_1-\sigma_2)q$	e^2	0	yes
	$^3P_1$	$\frac{\sqrt{6}}{4}f(\sigma_1+\sigma_2)q$	f^2	1	yes

Table 1.1: Allowed six amplitudes in nonmesonic decay process.

1.2 Nonmesonic decay rate

The nonmesonic decay process is described by six amplitudes provided that the initial ΛN system is of relative S-states[4]. They are listed in Table 1.1. Three amplitudes(c, d and e) have isospin $I_f = 0$ in the final NN system which give no contribution to the neutron stimulated decay($\Lambda + n \to n + n$). Since proton-neutron system has an isospin either 0 or 1, the six amplitudes contribute to the proton stimulated decay($\Lambda + p \to n + p$). Assuming the $\Delta I = 1/2$ rule holds in the nonmesonic decay, simple algebra on isospin gives the relation:

$$\{a_p,\ b_p,\ f_p\} = \sqrt{2}\{a_n,\ b_n,\ f_n\}, \tag{1.5}$$

where the suffixes p and n represent that the amplitudes are of proton- and neutron stimulated decays, respectively. Then the decay rates are given by

$$\Gamma_p = a^2 + b^2 + c^2 + d^2 + e^2 + f^2, \tag{1.6}$$

$$\Gamma_n = 2(a^2 + b^2 + f^2). \tag{1.7}$$

Important quantity is the Γ_n/Γ_p ratio represented as,

$$\frac{\Gamma_n}{\Gamma_p} = \frac{2\Gamma(I_f = 1)}{\Gamma(I_f = 0) + \Gamma(I_f = 1)}, \tag{1.8}$$

since the ratio is sensitive to the isospin structure of nonmesonic decay mechanism.

In the early 1960's, Block and Dalitz analyzed phenomenologically the decay rates of 4- and 5-body hypernuclei($^4_\Lambda$H, $^4_\Lambda$He and $^5_\Lambda$He) from emulsion data assuming

${}^{A}_{\Lambda}Z$	Γ_{NM}	Γ_n/Γ_p	comments	Refs.
${}^{4}_{\Lambda}$He	$(1.13 \pm 0.22) \times \Gamma_{\pi^-}$	0.27 ± 0.14	π^-, p, n measured	[5]
	$(0.51 \pm 0.16) \times \Gamma_{\pi^-}$	0.06 ± 0.40	π^-, π^0, p measured	[6]
${}^{5}_{\Lambda}$He	$(0.92 \pm 0.31) \times \Gamma_{\pi^-}$	0.93 ± 0.55	π^-, p, n measured	[7]
${}^{11}_{\Lambda}$B		$1.04^{+0.59}_{-0.48}$	π^0, p, n measured	[7]
	$(0.95 \pm 0.13 \pm 0.04) \times \Gamma_{\Lambda}$	$2.16 \pm 0.58^{+0.45}_{-0.95}$	π^-, p measured	[8]
${}^{12}_{\Lambda}$C	$(1.14 \pm 0.20) \times \Gamma_{\Lambda}$	$1.33^{+1.12}_{-0.81}$	π^-, p, n measured	[7]
	$(0.89 \pm 0.15 \pm 0.03) \times \Gamma_{\Lambda}$	$1.87 \pm 0.59^{+0.32}_{-1.00}$	π^-, p measured	[8]

Table 1.2: The counter-experimental data of Γ_{NM} and Γ_n/Γ_p.

$\Delta I = 1/2$ rule. They concluded that the ${}^3S_1 \to {}^3P_1$ amplitude($I_f = 1$) is dominant among the four amplitudes which have the initial ${}^3S_1$ state and that the contribution of the initial ${}^1S_0$ state is 1/2.6 compared to that of the initial ${}^3S_1$ state[4]. In 1980's, the counter experiments were carried at BNL and KEK[5, 6, 7, 8]. Results are summarized in Table 1.2. All the result except for the ${}^{4}_{\Lambda}$He indicates that the Γ_n/Γ_p's are 1–2. This also led to a conclusion that the $I_f = 1$ channel is dominant, although the experimental errors are quite large.

After the phenomenological analysis by Bolck and Dalitz, a one-pion exchange model was developed to describe the nonmesonic decay mechanism[9]. The model was extended later to one-meson exchange where the heavy mesons such as K, K^*, η, ρ and ω were included[10, 11, 12, 13]. Basic idea of one-pion exchange model is that the nonmesonic decay could be understood in terms of the the free Λ decay($\Lambda \to N\pi$) with the exception that the pion has to be considered virtual and is absorbed on a second nucleon bound in the hypernucleus. Most complete work so far has been done by Parreño et al.[13]. They included the exchange of the all heavy mesons. Also they included realistic ΛN short-range correlations and NN final state interactions and all the calculation was done in a shell model framework. Although the contribution of the kaon exchange modifies decay rates and their ratios drastically, the heavy meson contributions are canceled with each other. Then the calculation is mostly determined by the pion exchange. The strong tensor force in pion exchange potential makes ${}^3S_1 \to {}^3D_1$ amplitude($I_f = 0$) dominant in the six amplitudes. Calculated total decay rates of nonmesonic decay agreed with the experiment, however the ratios of Γ_n/Γ_p were far below the experiment, ~ 0.1.

Some theoretical work attempted to describe nonmesonic decays based on the direct quark exchange[14, 15, 16]. In this treatment, the interaction at short distance is described by a direct quark mechanism rather than the heavy meson exchange and superpose on one-pion exchange as a long range interaction. Inoue et al. found that the decay rate due to the direct quark exchange are comparable to that due to the one-pion exchange and moreover they predicted the large $\Delta I = 3/2$ amplitudes in initial $^1S_0$ state[16]. Note that there is difficulty to apply the model to actual cases, since the relative phase of the two amplitudes of the one-pion exchange and the quark exchange cannot be determined. Results for light hypernuclei showed that the total rates preferred a coherent sum while the ratio Γ_n/Γ_p was better reproduced with an incoherent sum. Thus either the quark exchange model or the meson exchange model alone is insufficient to describe nonmesonic decay mechanism.

Recently the validity of the $\Delta I = 1/2$ rule for the nonmesonic decay, which is a priori assumed in the meson exchange model, was tested from the experimental data of the 4- and 5-body Λ hypernuclei[17, 5, 6]. Nonleptonic weak decays of K meson and hyperons indicate that $\Delta I = 1/2$ transitions are greatly favored over $\Delta I = 3/2$ transitions by a factor 15–30. In the nonmesonic decay of Λ hypernuclei one can observe short-range effect since the momentum transfer is large as 400 MeV/c, hence the nonmesonic decay can provide information different from the other hadoronic decays. In the analysis the decay rates whose initial states is $^1S_0$ were extracted for both the proton- and neutron stimulated decays. The ratio of the decay rates, which corresponds to the factor 2 in Eq. 1.7, is varied by the ingredient of the $\Delta I = 3/2$ in the weak decay. Currently existing data has no sensitivity due to the large experimental errors[5, 6]. Further experiment will be carried at BNL[18].

1.3 Polarization of Λ hypernuclei

Prior to the description of the asymmetry of nonmesonic decay, I would like to mention the polarization of hypernuclei. The production of polarized hypernuclei was studied theoretically by Ejiri et al. at first[21]. They indicated that the hypernuclei can be polarized by the distortion effect of incoming and outgoing meson in the (π^+, K^+) and (K^-, π^-) reactions even though the spin-flip interaction amplitude is absent. In classical point of view, the direction of polarization due to the transferred orbital angular momentum is different between near-side and far-side reactions or between upstream and downstream reactions(Figure 1.1). The difference of the cross section in each side introduces the polarization of produced hypernuclei.

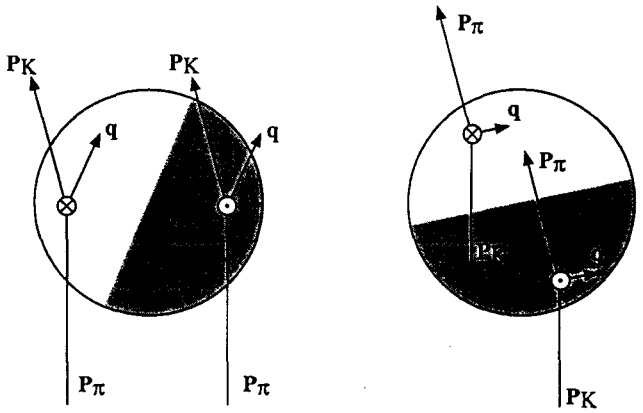

Figure 1.1: Schematic reaction diagrams for the polarization mechanism of Λ hypernuclear production by (π^+, K^+) reaction(left) and (K^-, π^-) reaction(right). $\odot$ and $\otimes$ indicate the upward and downward polarizations, respectively. q is the transfered momentum of the reactions.

The momentum transfer of the (K^-, π^-) reaction at $P_{K^-} = 750$ MeV/c is much smaller than that of the (π^+, K^+) reaction at $P_{\pi^+} = 1050$ MeV/c. The difference of the mean free path between incoming and outgoing mesons is smaller in the former reaction. Furthermore the elementary process $n(K^-, \pi^-)\Lambda$ for the incident K^- momentum below 800 MeV/c produces little spin polarization of the Λ[22]. Therefore the (π^+, K^+) reaction is suitable to produce the polarized hypernuclei. In Ref. [23], the polarization of hypernuclei produced by the (π^+, K^+) reaction was reformulated in terms of all elementary amplitudes[24]. The result of the polarization for the ground state of ${}^{12}_{\Lambda}$C is, for example, about 50% for $\theta_{K^+} = 10° - 15°$ at $P_{\pi^+} = 1.04$ GeV/c.

1.4 Asymmetry of nonmesonic decay

If a Λ is polarized, its decay products are emitted asymmetrically. Because of parity violating in the weak process, there are p-wave contribution as well as s-wave one. The asymmetric decay of Λ is due to the interference between s- and p-wave amplitudes. The asymmetry parameter is defined as

$$W(\theta) \propto 1 + \alpha P_\Lambda \cos\theta, \tag{1.9}$$

where W is an angular distribution of decay proton, P_Λ is a polarization of Λ and θ is an emission angle with respect to the Λ polarization. The asymmetry parameter

of free Λ decay is[19],

$$\alpha_p^{free} = 0.642 \pm 0.013. \tag{1.10}$$

Parity violation of the weak nonmesonic decay also causes the asymmetric emission of decay particle with respect to the Λ polarization. The asymmetry parameter is expressed as[20],

$$\alpha_p^{NM} = \frac{\frac{\sqrt{3}}{2}(\sqrt{2}c + d)f}{\frac{1}{4}\{a^2 + b^2 + 3(c^2 + d^2 + e^2 + f^2)\}}, \tag{1.11}$$

where a to f are the amplitudes in Table 1.1. Amplitudes f and d represent dominantly kaon and pion exchange, respectively and are suggested to be dominant from experiments and meson exchange model, respectively. Therefore the study of the asymmetry parameter elucidates dominant part of the nonmesonic decay mechanism.

Recently the experiment to measure the asymmetry parameter of the nonmesonic weak decay was carried out at KEK(PS-E160)[25]. In the experiment, a ${}^{12}_{\Lambda}\mathrm{C}$ was produced by a ${}^{12}\mathrm{C}(\pi^+, K^+)$ reaction. Because a p-substitutional state, $(p_{3/2})_n^{-1}(p_{3/2})_\Lambda$, is above the proton decay threshold, its decay into a ${}^{11}_{\Lambda}\mathrm{B}$ before the weak decay is occurred(see Figure 1.2). Observed asymmetry[26] are summarized in Figure 1.3. In order to obtain polarization of hypernuclei to decay, first the polarization of hypernuclear states produced by the (π^+, K^+) reaction was evaluated[23, 27]. Then depolarization in the particle and γ deexcitation process was calculated[28]. Unfortunately, the ground state of ${}^{12}_{\Lambda}\mathrm{C}$ has the polarization of only 5–7% at decaying stage due to the M1 transition of low-lying 1^- states to ground state, although the polarizations at reaction stage are sizable. Experimental results were reduced to a common value for the asymmetry parameter of $\alpha_p^{NM} = -1.3 \pm 0.4$ for the p-shell hypernuclei as shady region in Figure 1.3. Qualitatively, the obtained asymmetry parameter suggests equal importance of the final isospin $I_f = 0$ and $I_f = 1$ amplitudes and seems to contradict the phenomenological analysis of branching ratio[4], where the $I_f = 1$ amplitude is dominated. The theory based on the one meson exchange model predicts the asymmetry parameter of $-0.3 \sim -0.4$ for p-shell hypernuclei[13] and the direct quark exchange model predicts $-0.2 \sim 0.2$[16]. However the detailed comparison with these calculations is impossible because the experimental value has large errors and there is no experimental support to the calculated polarization.

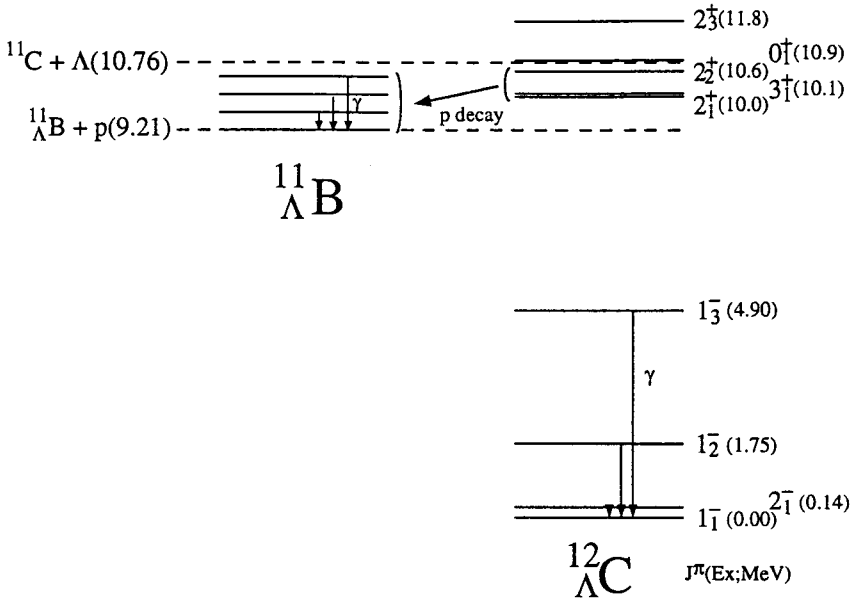

Figure 1.2: Level scheme of low-lying $^{12}_{\Lambda}$C is shown. Excitation energies of the levels were quoted from Ref. [27].

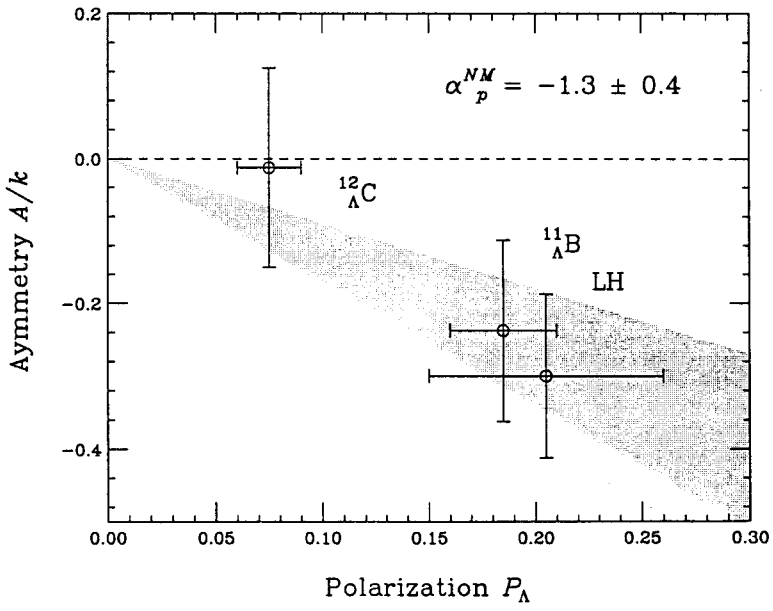

Figure 1.3: The observed asymmetries A_1/k_pP_Λ, with $k = 0.8$ being the attenuation factor due to the intranuclear cascade process, versus the evaluated polarization P_Λ. The shady region of $\alpha_p^{NM} = -1.3 \pm 0.4$ is derived from the data.

1.5 KEK PS-E278 experiment

Previous experiment demonstrated the large asymmetry parameter for the weak nonmesonic decay of ${}^{12}_{\Lambda}$C. However the polarization of hypernuclei was not measured in the experiment. The p-wave contribution in the initial ΛN state of the nonmesonic decay makes the discussion of the decay mechanism indirect. Thus it is highly desired to measure the asymmetry parameter with less ambiguity. We report in this thesis on an experiment which has been carried out at KEK(PS-E278)[29] to measure the weak decay of ${}^{5}_{\Lambda}$He hypernucleus.

The ^{6}Li$(\pi^+, K^+){}^{6}_{\Lambda}$Li reaction was employed to produce ${}^{5}_{\Lambda}$He. A level scheme of ${}^{6}_{\Lambda}$Li is shown in Figure 1.4. The ground state of ${}^{6}_{\Lambda}$Li lies above the threshold of ${}^{5}_{\Lambda}\mathrm{He} + p$. The produced ${}^{6}_{\Lambda}$Li decays into ${}^{5}_{\Lambda}$He with emitting proton if the Λ produced in s orbit, while the Λ escapes if the Λ produced in p orbit. This decay mechanism of ${}^{6}_{\Lambda}$Li was confirmed experimentally by in-flight (K^-, π^-) experiment at BNL[7]. The mass spectra obtained in the experiment are shown in Figure 1.5. p-substitutional state is diminished in the spectrum gated by decay proton which is the signature of hypernuclear production, while the ground state and s-substitutional state are enhanced. Since there is no low-lying excited state in ${}^{5}_{\Lambda}$He, The ground state of ${}^{6}_{\Lambda}$Li exclusively produces the ground state of ${}^{5}_{\Lambda}$He.

The cross section and the polarization have been calculated for the ^{6}Li(π^+, K^+) reaction at 1.05 GeV/c[31]. Although there is an ambiguity due to the structure of ${}^{6}_{\Lambda}$Li, the polarization of ${}^{5}_{\Lambda}$He in the ground state region is expected to be 0.25–0.5 at the scattering angle of $\theta_K = 10 - 18°$. This value is 1.5$\sim$2 times larger than that of ^{12}C(π^+, K^+) case. The polarization of ${}^{5}_{\Lambda}$He is equal to that of Λ in a nucleus since the spin-parity of ^{4}He core is 0^+. Thus there is no ambiguity to derive the Λ spin polarization in the nucleus.

The Λ polarization is necessary to extract the asymmetry parameter of the nonmesonic decay with Eq. 1.9. For the ${}^{12}_{\Lambda}$C and ${}^{11}_{\Lambda}$B cases, there was no way to obtain the polarization experimentally and the theoretical calculation was employed. In the present experiment, the asymmetry of mesonic decay of ${}^{5}_{\Lambda}$He can be used to determine the polarization of ${}^{5}_{\Lambda}$He. The asymmetry parameter of mesonic decay of ${}^{5}_{\Lambda}$He is expected to be almost same as that of free Λ decay[31]. The large branching ratio($\Gamma_{\pi^-}/\Gamma_{\Lambda} = 0.44 \pm 0.11$[7]) and large asymmetry parameter($\alpha_{\pi^-}^{free} = -0.642 \pm 0.013$[19]) gives the polarization of ${}^{5}_{\Lambda}$He with enough precision to derive the asymmetry parameter of the nonmesonic decay.

Since the nonmesonic decay is occurred inside the nuclear matter, the effect of final state interaction cannot be avoided. The correction on the asymmetry

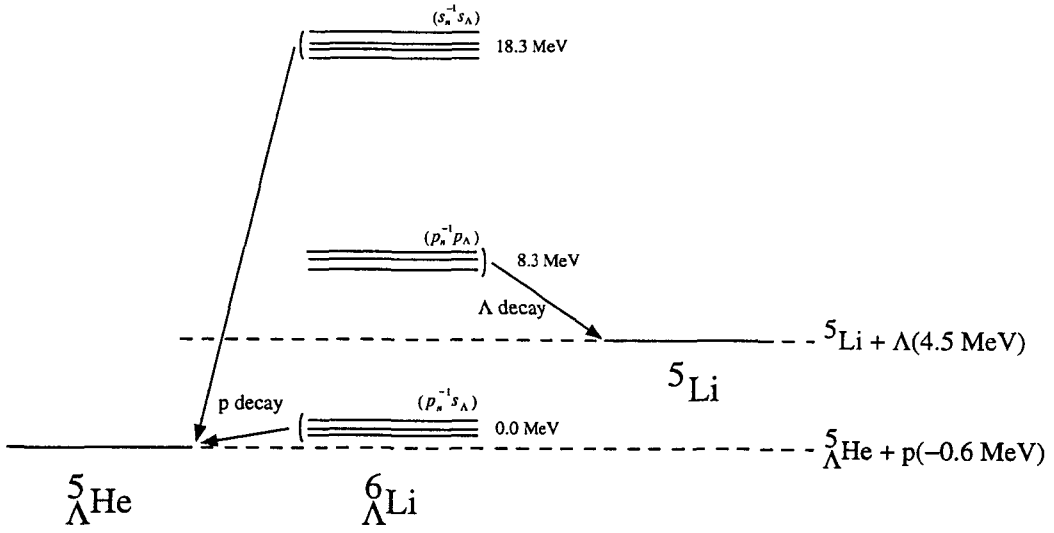

Figure 1.4: Level scheme of $^6_\Lambda$Li is shown. Energies are quoted from Ref. [30].

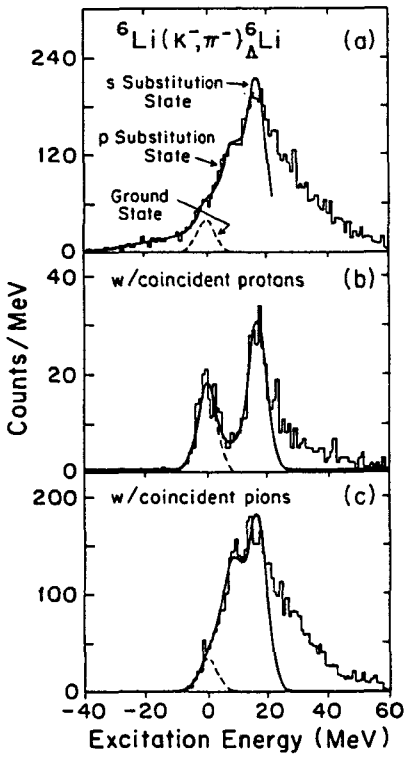

Figure 1.5: Hypernuclear mass spectra obtained by ^{6}Li(K^-,π^-) reaction[7].

parameter due to Fermi motion and intranuclear cascade is estimated to 5% which is much smaller than 20% for ${}^{12}_{\Lambda}$C case[32].

The features of the measurement of ${}^{5}_{\Lambda}$He are listed below.

- The expected polarization is 1.5~2 times larger than the previous ${}^{12}_{\Lambda}$C experiment.
- Polarization of Λ in ${}^{5}_{\Lambda}$He is unambiguously equal to that of ${}^{5}_{\Lambda}$He
- Polarization of the ${}^{5}_{\Lambda}$He can be given by observing the asymmetry of pions from the mesonic decay of ${}^{5}_{\Lambda}$He. In the previous experiment theoretical calculation was employed to derive the Λ polarization.
- The effect of final state interaction on observed asymmetry is small as 5%, while that is 20% for ${}^{12}_{\Lambda}$C case.
- There is only a relative s-wave in initial ΛN system of the nonmesonic decay, since the ${}^{5}_{\Lambda}$He is a s-shell hypernucleus. This makes the comparison with theoretical calculation simple.

These superior features promise to improve the measurement of asymmetry parameter of the nonmesonic decay.

The purpose of the present experiment is to obtain

(1) the polarization of the ${}^{5}_{\Lambda}$He by observing the asymmetry of the mesonic decay,

(2) the asymmetry parameter of the ${}^{5}_{\Lambda}$He nonmesonic decay and

(3) the branching ratio of the mesonic and nonmesonic decay.

In this thesis, We focus on the asymmetry of the ${}^{5}_{\Lambda}$He weak decay and present the results of the subjects (1) and (2) above. Chapter 2 describes the experimental apparatus. In Chapter 3, the procedures for the data analysis are described. The results are presented in Chapter 4. The results are discussed in Chapter 5. Concluding remarks are given in Chapter 6.

Chapter 2

Experimental Apparatus

The experiment, KEK-PS E278, to measure the asymmetry of decay pions and protons from the polarized ${}^{5}_{\Lambda}$He was carried out at the K6 beam line of 12 GeV proton synchrotron in KEK. The ^{6}Li(π^+, K^+) reaction at P_π=1.05 GeV/c was used to produce polarized ${}^{6}_{\Lambda}$Li. The momenta of scattered kaons were measured by the SKS spectrometer which was developed by the collaboration of INS and KEK for previous experiment, E140a. The SKS covered the scattering angle from -18 to 18 degrees enough to introduce polarization to the Λ hypernucleus.

Decay particles were detected by two symmetric counter systems above and below the target. Each counter system consisted of Silicon Strip Detectors(SSD), MultiWire Proportional Chamber(MWPC), Range Shower Counter(RSC) and 36 NaI detectors and covered 30% of the total solid angle. RSC consisted of 32 sets of plastic scintillator sheet(1 mm) and lead sheet(0.2 mm) to measure both the total energy and the range of decay particles. The energy loss information measured by SSD was used for identification of decay protons and pions with the total energy and the range information. The tracking information from SSD and MWPC was used for the correction of the path length in SSD and RSC. NaI detectors are used for π^0 detection.

This chapter describes the experimental apparatus of E278 experiment.

2.1 K6 beam-line

The K6 beam line is a general-purpose high-intensity beam line which can supply various mass-separated secondary beams in the momentum range between 0.5 and 2 GeV/c[33]. The primary proton beam was extracted for 1.7 sec in each 4.0 sec synchronized to the KEK 12GeV PS operation cycle. The secondary pion beam was

Momentum range	0.6–2.0 GeV/c
Production target	Pt(ϕ6 mm $\times$ 60 mm)
Central production angle	0°
Beam length	30.0 m
Solid angle acceptance	1.9 msr
	$\pm$60 mrad(H), $\pm$10 mrad(V)
Momentum bite($\Delta p/p$)	$\pm$2.4%
Electrostatic separator	length 6 m, gap 10 cm
	field 40 kV/cm
Beam characteristics at the beam end:	
Magnification	-1.1(H), -1.4(V)
Dispersion	0.34(cm/% $\Delta p/p$)
Image size	0.4 cm(H), 0.9 cm(V)
Divergence	$\pm$57 mrad(H), $\pm$3.6 mrad(V)
$\pi^+(\pi^-)$ Yield at 1 GeV/c	$\sim 10^7/10^{12}$ primary protons

Table 2.1: Parameters of the K6 beam line.

produced on a production target. A platinum rod of $\phi 6 \times 60$ mm^2 was used as the production target in this experiment. Figure 2.1 shows a schematic view of the K6 beamline. The beamline is comprised of two dipole magnets(D1, D2), ten quadruple magnets(Q1–Q10), a sextuple magnet(SX), an electrostatic separator(DC separator) with two correction magnets(CM1, CM2), and four slits. The slits are installed between D1 and Q1(acceptance slit), between Q2 and Q3(intermediate focus slit), between SX and Q5(momentum slit), and between Q6 and Q7(mass slit). The parameters of the K6 beam line are summarized in Table 2.1.

Figure 2.2 shows the beam envelopes calculated with TRANSPORT[34] for the (π^+, K^+) beam-transport condition. It is a special feature of the K6 beamline that there is a vertical focus point at the intermediate focus slit to reduce the background beam halos. The beam was achromatically focussed at the experimental target. The measured beam size was typically 6.0(H)$\times$7.5(V) mm^2 in rms.

The central beam momentum was set at 1.05 GeV/c where the cross section of the elementary $n(\pi^+, K^+)\Lambda$ process is almost at maximum(Figure 2.3). The measured momentum distribution is shown in Figure 2.4. The beam intensity at the experimental target was 3.0×10^6/spill. The proton and positron contaminations in the beam were measured to be typically 10 and 4%, respectively. The muon

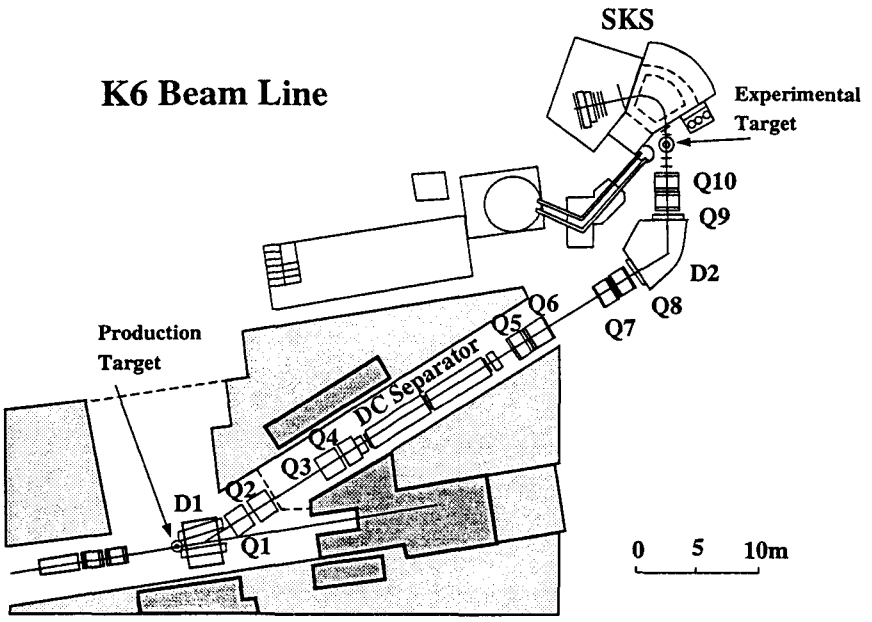

Figure 2.1: Schematic view of the K6 beam line of KEK 12GeV PS.

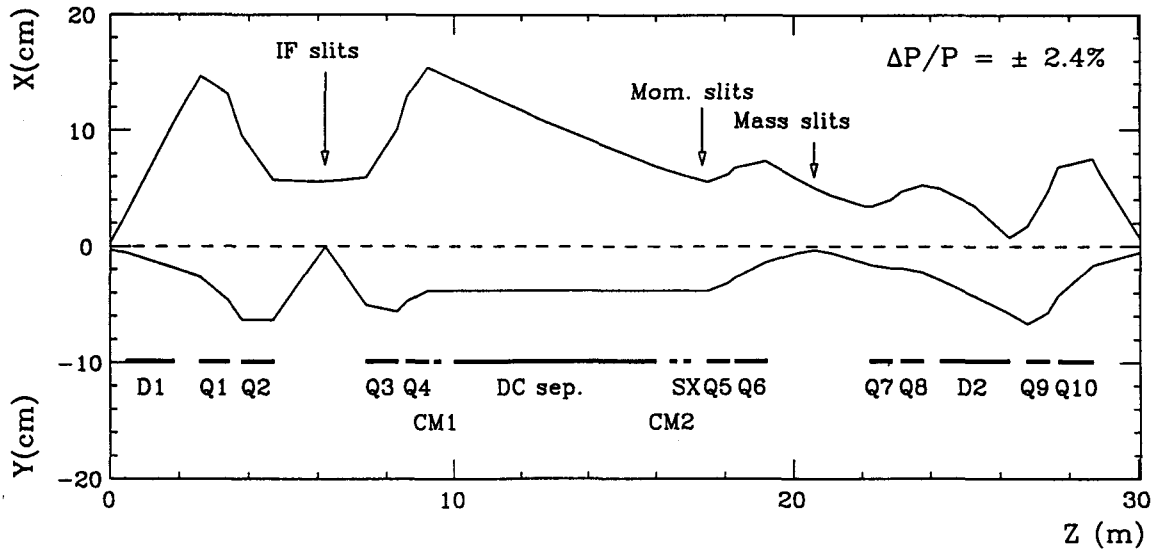

Figure 2.2: Beam envelope of the K6 beamline for the (π^+, K^+) beam-transport condition calculated by TRANSPORT.

Name	Plane	Tilt Angle	Drift space (mm)	Active Area H×V (cm^2)	Resolution (σ mm)
BDC1	$x - x'$	0°	2.5	24.0×15.0	0.35
	$u - u'$	−15°	2.5	24.0×15.0	0.35
	$v - v'$	15°	2.5	24.0×15.0	0.35
BDC2	$v - v'$	15°	2.5	24.0×15.0	0.35
	$u - u'$	−15°	2.5	24.0×15.0	0.35
	$x - x'$	0°	2.5	24.0×15.0	0.35
BDC3	$x - x'$	0°	2.5	24.0×15.0	0.35
	$u - u'$	−15°	2.5	24.0×15.0	0.35
	$v - v'$	15°	2.5	24.0×15.0	0.35
BDC4	$v - v'$	15°	2.5	24.0×15.0	0.35
	$u - u'$	−15°	2.5	24.0×15.0	0.35
	$x - x'$	0°	2.5	24.0×15.0	0.35

Table 2.2: Specifications of the beam drift chambers.

contamination was measured as 6% in E140a experiment[35].

2.2 Beam Spectrometer

The beam spectrometer system consisted of a QQDQQ magnet system with four sets of drift chambers(BDC1∼4) and trigger counters(Figure 2.5). The trigger counters comprise a Freon-gas Čerenkov counter(GC) for positron rejection, a segmented scintillation counter(BH) and beam defining scintillation counter(BS). BS was used as time-zero counter. The proton contamination in beam was rejected by Time-Of-Flight(TOF) between BH and BS in on-line trigger.

The beam momentum was measured by the QQDQQ system with the drift chambers by using a transport matrix, particle by particle. In order to minimize the multiple scattering effect on the momentum resolution, the $(x|\theta)$ term of the transport matrix was tuned to be zero to the first order. A vacuum chamber was installed between BDC2 and BDC3 in the magnets. In addition, the tracking drift chambers were made as thin as possible in substance.

Specifications of the beam drift chambers are shown in Table 2.2. The four chambers have the same structure as that shown in Figure 2.6. To be used under a high counting rate, the sense-wire spacing was made to be short(5 mm), as shown in

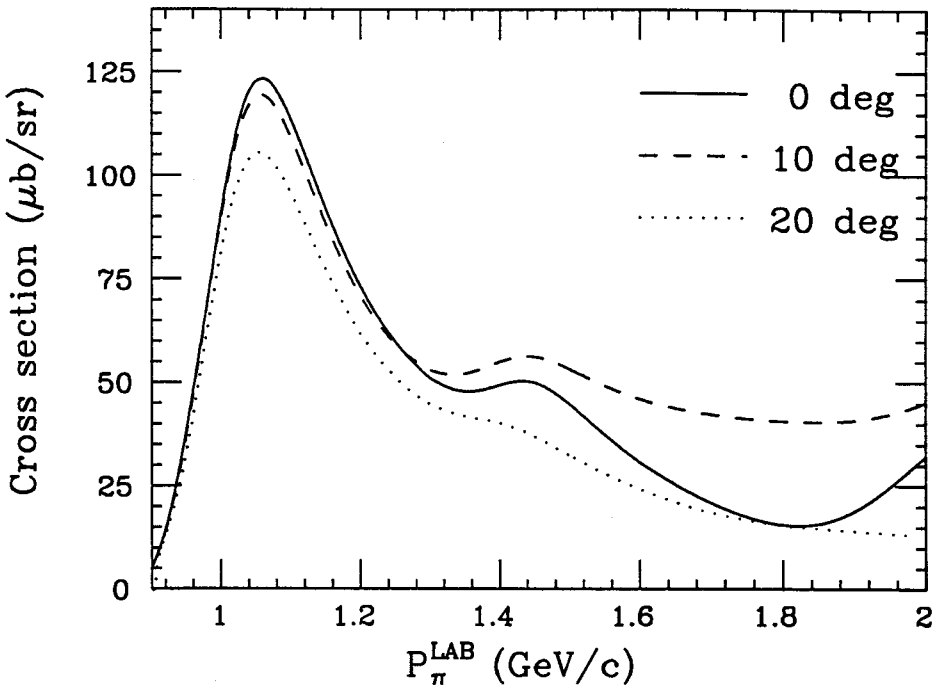

Figure 2.3: Cross section of the elementary $n(\pi^+, K^+)\Lambda$ process[24].

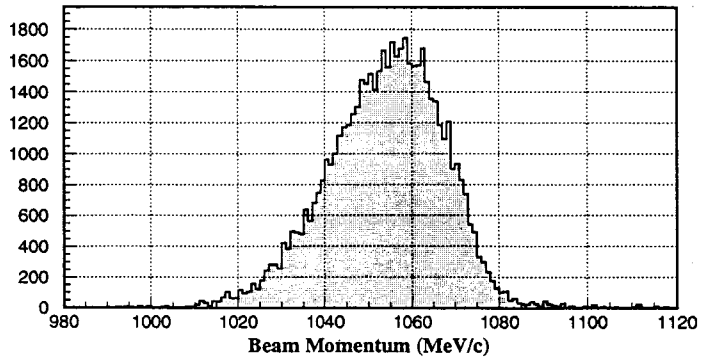

Figure 2.4: Momentum distribution at the experimental target measured for a 1.05 GeV/c π^+ beam.

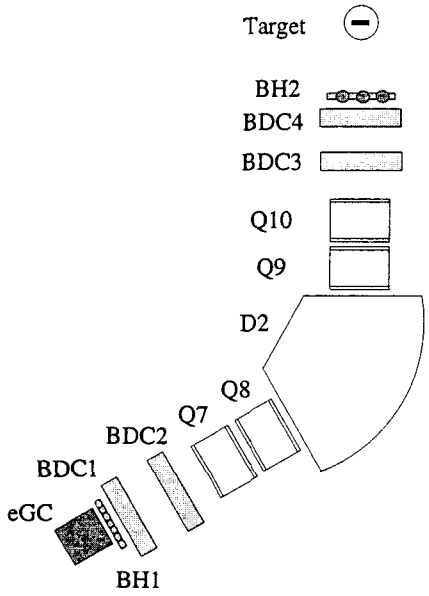

Figure 2.5: Schematic view of the beam spectrometer system.

Figure 2.8. Each chamber included six layers of sense-wire planes($xx'uu'vv'$), where vertical and $\pm 15°$ tilted wire planes are denoted by x, u and v, respectively. The primed planes were placed at the position shifted half-cell from accompanied planes in order to solve the left right ambiguity.

The sense and potential wires were made of gold-plated tungsten($\phi 12.5\mu$m) and gold-plated copper beryllium($\phi 50\mu$m), respectively. The cathode planes were made of $7.5\mu m$ kapton foils coated with 0.1μm aluminum on both sides and 0.0015μm chromium for preventing oxidization of the aluminum coating. The gas mixture was Ar(79%)+C_4H_{10}(17%)+Methylal(4%) at atmosphere pressure.

The read-out electronics of the pre-amplifier and the amplifier/discriminator are equipped with two-stage pole-zero cancellation and one baseline restorer for a high-rate capability(Figure 2.7). A typical intrinsic resolution was $\sigma = 350\mu$m for one plane as shown in Figure 2.9, although the design value of the resolution is 250 μm. The figure shows the sum of drift length for a pair planes, where the width of peaks represents $\sqrt{2}$ times the intrinsic resolution.

Specifications of the three trigger counters are given in Table 2.3. BH was divided into seven vertical segments(Figure 2.10) in order to reduce the counting rate of each segment. The photomultipliers attached to the BH had additional high voltage(HV) supplier, so-called booster, on last three dinode stages besides of the main HV supplier to keep their gain under the high counting rate.

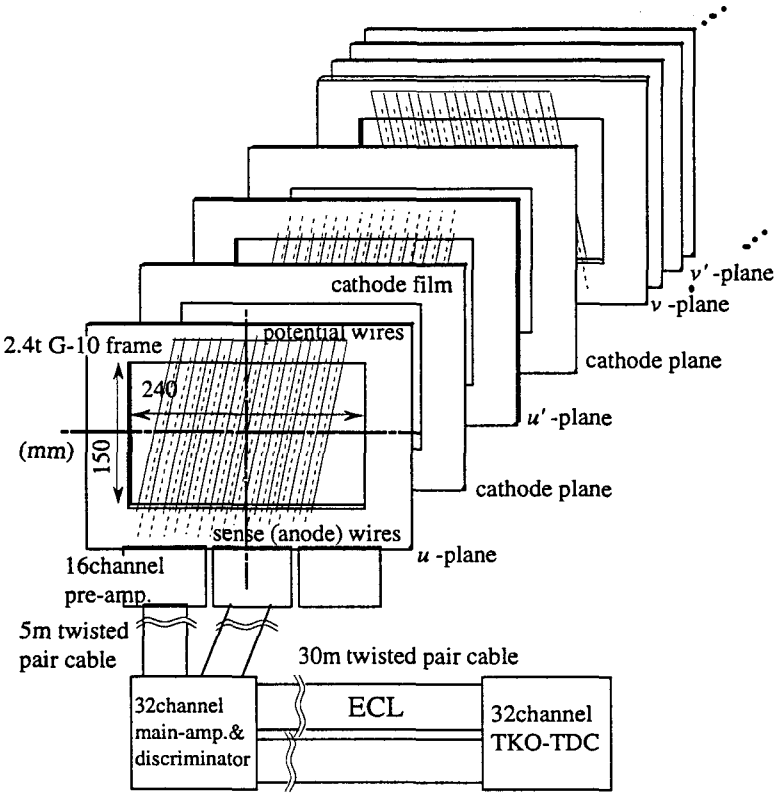

Figure 2.6: Schematic figure of the beam drift chamber and the readout system.

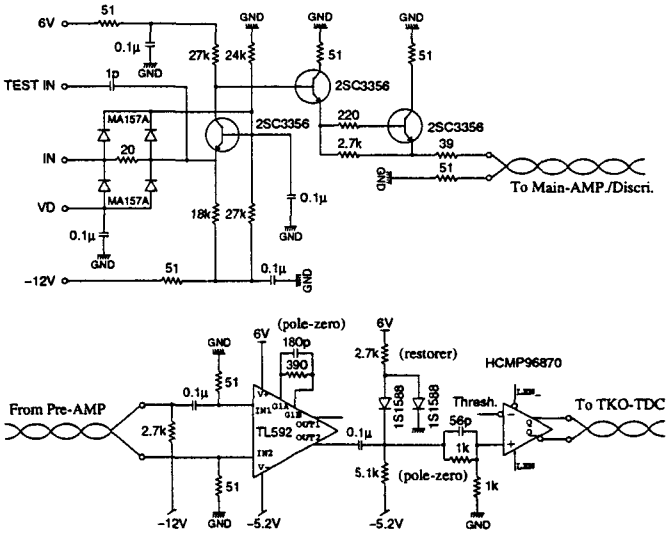

Figure 2.7: Schematic diagram of the pre-amplifier and the amplifier/discriminator module.

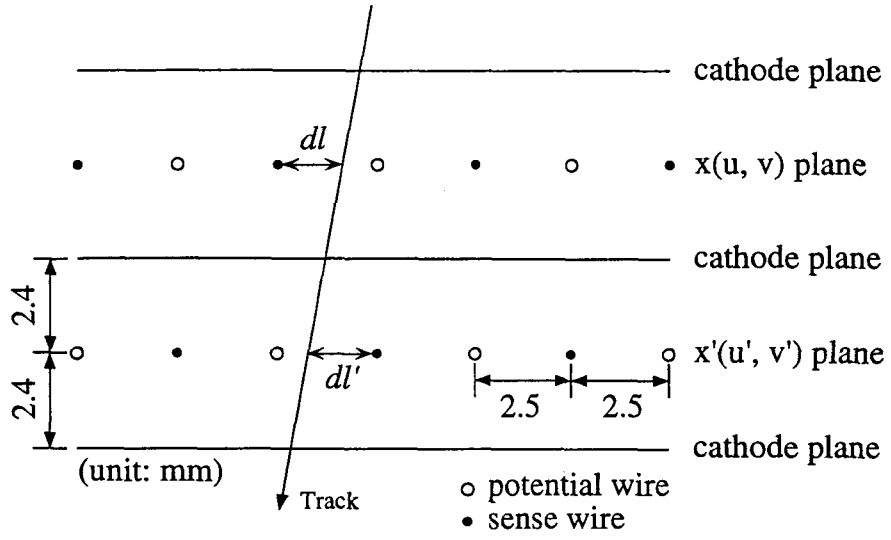

Figure 2.8: Cell structure of the beam drift chambers.

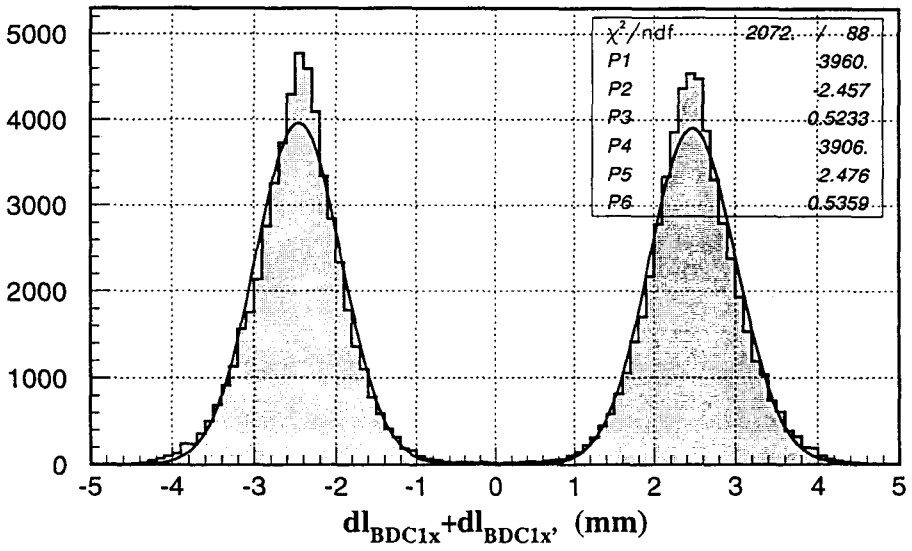

Figure 2.9: Typical distribution of the sum of the drift length for pair planes measured for a 720 MeV/c π^+ beam.

Name	Material	PMT	Volume(cm)	etc.
GC	Freon gas	R1584-02	$\phi 20 \times 29(L)$	n=1.00245
BH	Plastic	R1450	19(H)×9(V)×0.5(T)	7 segments
				3-stage-booster
BS	Plastic	H3173	4(H)×2(V)×0.5(T)	2-stage-booster

Table 2.3: Specifications of the beam trigger counters.

Momentum resolution	0.1 % FWHM at 720 MeV/c
Maximum central momentum	1.1 GeV/c
Bending angle	100°(central trajectory)
Momentum acceptance	±10 %
Angular acceptance	100 msr
Flight path	~5 m(central trajectory)

Table 2.4: Design parameters of the SKS spectrometer.

The beam defining counter, BS, was used as the time-zero counter. Although it was not segmented, it is sufficiently good time resolution(~ 200 psec) with booster on last two dinode stages, because the transmission of QQDQQ magnet was about 1/3 in typical (π^+, K^+) run. Figure 2.11 shows the TOF spectrum between BH and BS in (π^+, K^+) run. The width of peak represents time resolution of both counters. K^+ peak in the figure come from the background $(K^+, K^{+\prime}X)$ process which was enhanced due to the K^+ tagging system of scattered spectrometer.

2.3 Scattered particle spectrometer

The superconducting kaon spectrometer(SKS) was designed and constructed for the purpose of studying Λ hypernuclei via the (π^+, K^+) reaction[36]. In order to perform the spectroscopy with high statistics, it has outstanding characteristic features such as a good momentum resolution(0.1% FWHM) and a large angular acceptance(100 msr) as shown in Table 2.4.

Figure 2.12 shows schematic views of SKS. The spectrometer comprises a sector-shape superconducting dipole magnet with five sets of drift chambers(SDC1~3,4XY) for momentum measurement and three kinds of trigger counters for particle identification: a scintillation counter wall(TOF), two silica aerogel Čerenkov counters(AC1

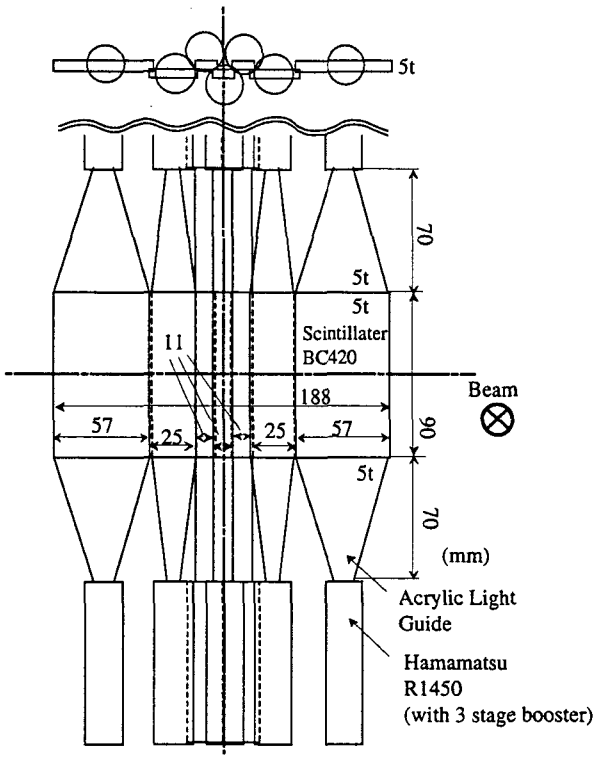

Figure 2.10: Schematic view of the BH.

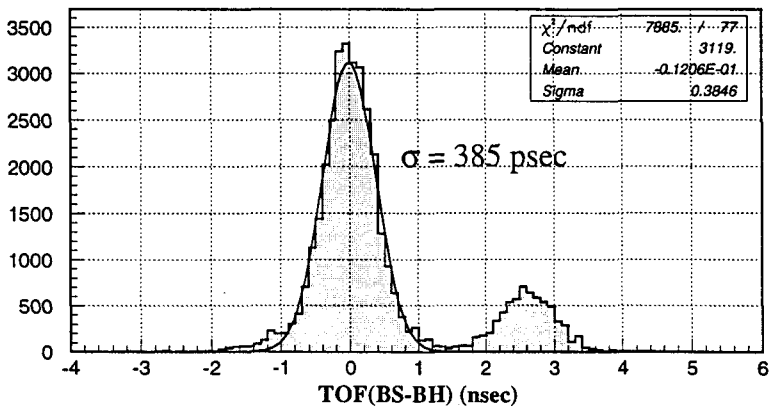

Figure 2.11: TOF spectrum between BH and BS in (π^+, K^+) run.

Maximum magnetic field	3 T
Maximum field on conductors	4.5 T
Stored energy	10.6 MJ
Pole gap	49.75 cm
Coil cross section	15×12 cm^2
Conductor	NbTi/Cu
Ampere turns	2.1 MA·T
Maximum current	500 A
Inductance	86.9 H
Cold mass coil	4.5 t
Shield	0.44 t
Weight of yoke	263 t
Total weight	280 t
Heat lead at 4 K	5 W
Content of liquid He	156 L

Table 2.5: Parameters of the SKS magnet.

and AC2), and Lucite Čerenkov counter wall(LC).

In order to realize a large acceptance and a good momentum resolution, the configuration of a single sector-shape superconducting dipole magnet with a large aperture was adopted[37, 38]. Unlike a conventional high resolution spectrometer used in nuclear physics, there are no precise focus planes. The parameters of the SKS magnet are summarized in Table 2.5. Under (π^+, K^+) condition, the magnet was operated in the 2.2 T mode(272 A), where the central trajectory corresponded to 0.72 GeV/c.

The momentum was determined by reconstructing a particle track with the Runge-Kutta tracking method[39] particle by particle using a magnetic field map measured prior previous E140 experiment. Table 2.6 shows specifications of the drift chambers. Since SDC1 and SDC2 were exposed to the beam, the cell structure of them was the same as that of BDC, which were designed to be used under a high counting rate. A typical intrinsic resolution was $\sigma = 250\mu$m for one plane as shown in Figure 2.13.

The sizes of SDC3, SDC4X and SDC4Y are larger in order to match the large angular and momentum acceptances. The SDC3 has only one plane to measure horizontal position(x) so as to make it as thin as possible. The SDC4X and SDC4Y have six sense wires in a cell, as shown in Figure 2.14. In each cell, the sense wire are staggered by ± 200 μm in order to solve left right ambiguity. The staggering

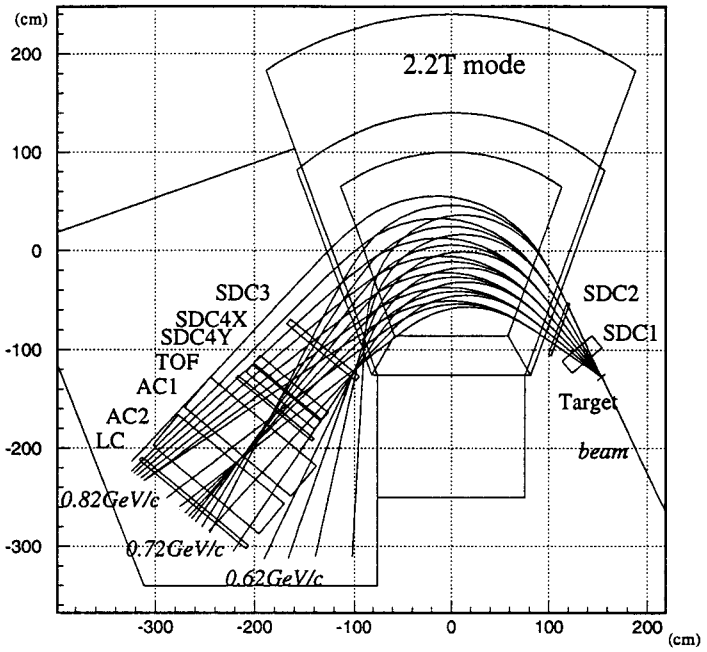

Figure 2.12: Schematic top view of SKS.

Name	Plane	Tilt Angle	Drift space (mm)	Active Area H×V (cm^2)	Resolution (σ mm)
SDC1	$x - x'$	0°	2.5	40.0×15.0	0.25
	$u - u'$	−15°	2.5	40.0×15.0	0.25
	$v - v'$	15°	2.5	40.0×15.0	0.25
SDC2	v	15°	2.5	56.0×15.0	0.25
	$x - x'$	0°	2.5	56.0×15.0	0.25
	v'	15°	2.5	56.0×15.0	0.25
SDC3	x	0°	21.0	100.0×100.0	0.25
SDC4X	x	0°	21.0	100.0×100.0	0.25
SDC4Y	y	90°	21.0	100.0×100.0	0.25

Table 2.6: Specifications of the scattered particle drift chambers.

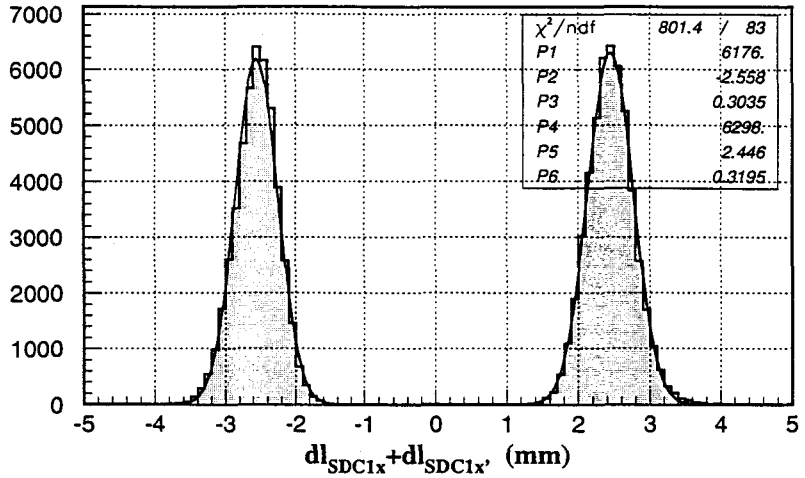

Figure 2.13: Typical distribution of the sum of the drift length for pair planes measured for a 720 MeV/c π^+ beam.

of the sense wire can be clearly seen in Figure 2.15. This figure shows a distribution of $(\Delta L_3 + \Delta L_5)/2 - \Delta L_4$ in SDC4X, where ΔL_n represents the drift length of the n-th sense wires in a cell. The two peaks correspond to the left and right hand sides of the sense wires. The width of a peak represents the intrinsic position resolution(typically $\sigma = 250\mu$m). The sense and the other wires are made of gold-plated tungsten($\phi 20\mu$m) and gold-plated aluminum($\phi 80\mu$m), respectively. The gas mixture for SDC3, SDC4X and SDC4Y is Ar(50%)+C_2H_6(50%) at atmosphere pressure. The two outermost sense wires in a cell had worse resolution than the other wires since they were noisier because of their incomplete field shape. The readout system was the same as that for BDC.

Table 2.7 shows specifications of the trigger counters for the scattered particles. In the trigger, a combination of three kinds of Čerenkov counters discriminate π, K and p; BLC and AC for π/K, LC for K/p. On the other hand, in the offline analysis, the time-of-flight measurement between TOF wall and BS offers the finest event selection. Furthermore, the ADC data were used for particle identification at the first stage of analysis.

Figure 2.16 shows a schematic view of the TOF counter, a scintillation counter wall comprising fifteen independent vertical segments. Fast photomultiplier are attached to both ends of a segment. Figure 2.17 show a time-of-flight spectrum between BS and TOF wall measured a 0.72 GeV/c π^+ beam with a correction of the momentum and the flight path in SKS. A typical time resolution is 200 psec in rms,

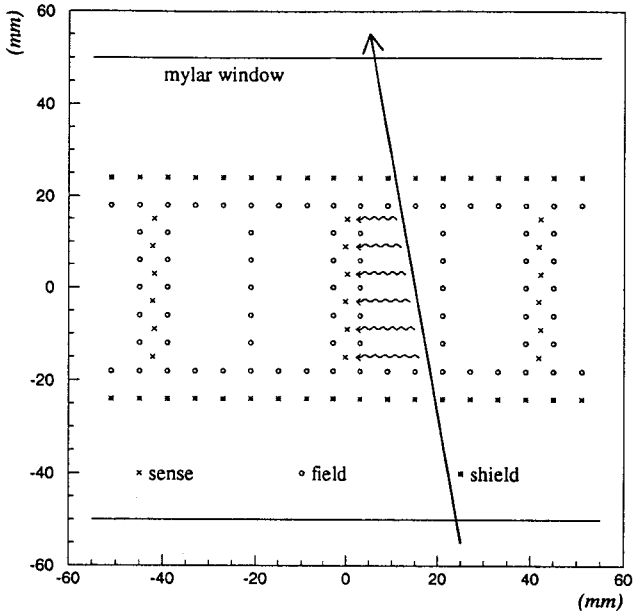

Figure 2.14: Wire configuration of SDC4X and SDC4Y. The sense wires are staggered by 200 μm to left- or right-hand sides alternatively.

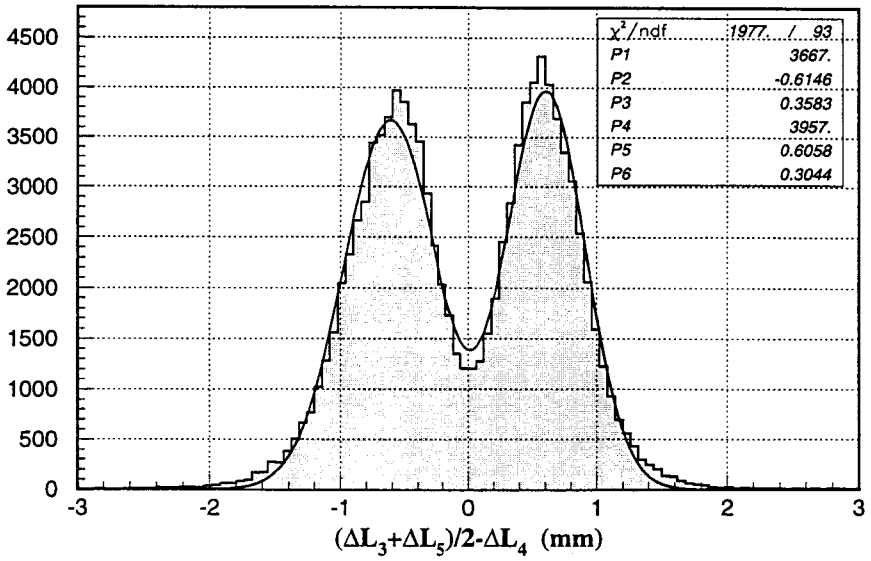

Figure 2.15: Distribution of $(\Delta L_3 + \Delta L_5)/2 - \Delta L_4$ of SDC4X measured for a 720 GeV/c π^+ beam. ΔL_n represents the drift length of the n-th sense wires in a cell.

Name	Material	PMT	Volume(cm)	etc.
BLC	Lucite	H3173(UV)	25.6(H)×6(V)×1(T)	n=1.49
TOF	Plastic	H1949	105(H)×100(V)×3(T)	15 segments
AC1	Aerogel	R1584-02	105(H)×120(V)×9(T)	n=1.06
AC2	Aerogel	R1584-02	140(H)×140(V)×12(T)	n=1.06
LC	Lucite	H1949	140(H)×140(V)×4(T)	n=1.49, 14 segments

Table 2.7: Specifications of the beam trigger counters.

including that of the two counter and the time jitter of the circuit modules. The timing offset parameters were determined in the off-line analysis using π^+ beam data periodically measured; they were found to be stable in each experimental cycle. The photomultiplier gains were stable during the experiment.

Figure 2.18 shows a schematic view of the AC1 counter. The structure of AC2 is essentially the same as that of AC1, except for the sizes. These are threshold type Čerenkov counters and veto pions with a threshold of 0.4 GeV/c. The refractive index was set to be 1.06 so as to fit the momentum region. The inner surfaces of the counter boxes were covered with aluminized mylar sheets[40]. In general, for π/K separation in the 1 GeV/c momentum region, the refractive index must be just between those of gas and liquid, as shown in Figure 2.19. Silica aerogel is an irreplaceable solid material as a Čerenkov radiator filling this refractive index range. Although liquid helium and liquid hydrogen have appropriate refractive indexes, they are hard to handle.

Figure 2.20 shows a schematic view of the LC counter. It was a threshold type Čerenkov counter comprising fourteen independent vertical segments. Protons were discriminated from pions and kaons using this counter. The threshold momentum for protons is about 0.85 GeV/c. In order to reduce the position dependence of the pulse height, the lucite contained 10 ppm of wavelength shifter(bis-MSB), by which directional Čerenkov photons were diffused. Because the wavelength shifter scintillates, LC is slightly sensitive to protons: typically 10% at 0.7 GeV/c.

The previous E140a experiment measured only inclusive spectra of the (π^+, K^+) reaction although the data taking rate was close to the limit of the ability of the data taking system employed. In the present experiment, we have twice more volume of target and twice more data from the decay counter system. Therefore it was important to reduce the trigger rate more tightly. The background was mainly related to the beam π^+ which reacted on the yoke of SKS magnet as well as on

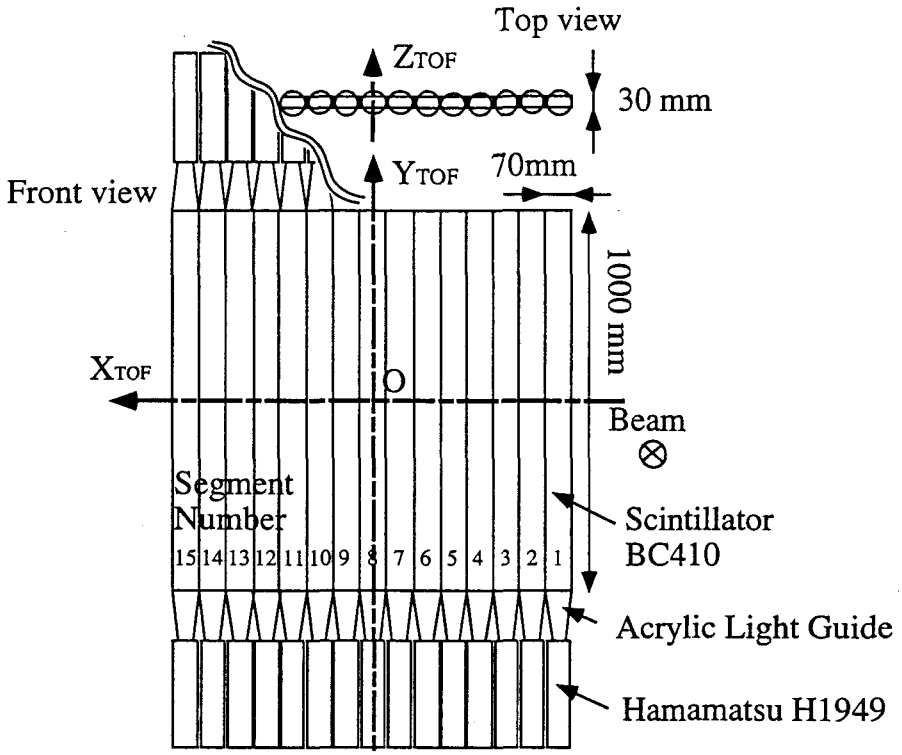

Figure 2.16: Schematic view of the TOF wall.

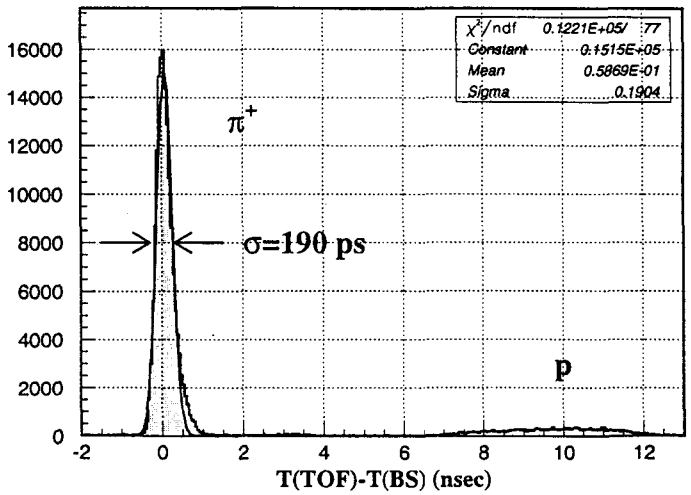

Figure 2.17: TOF spectrum between BS and TOF for a 720 MeV/c π^+ beam corrected with a flight path and momentum obtained by SKS tracking.

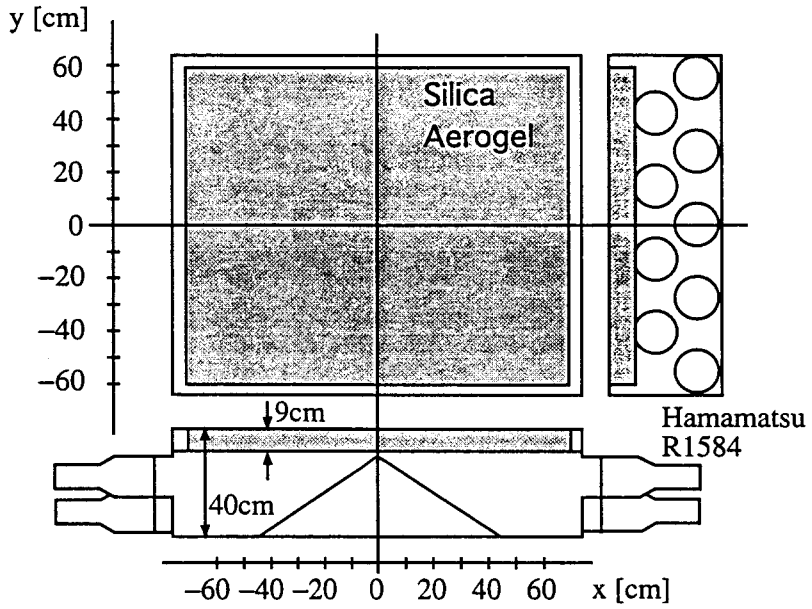

Figure 2.18: Schematic view of AC1.

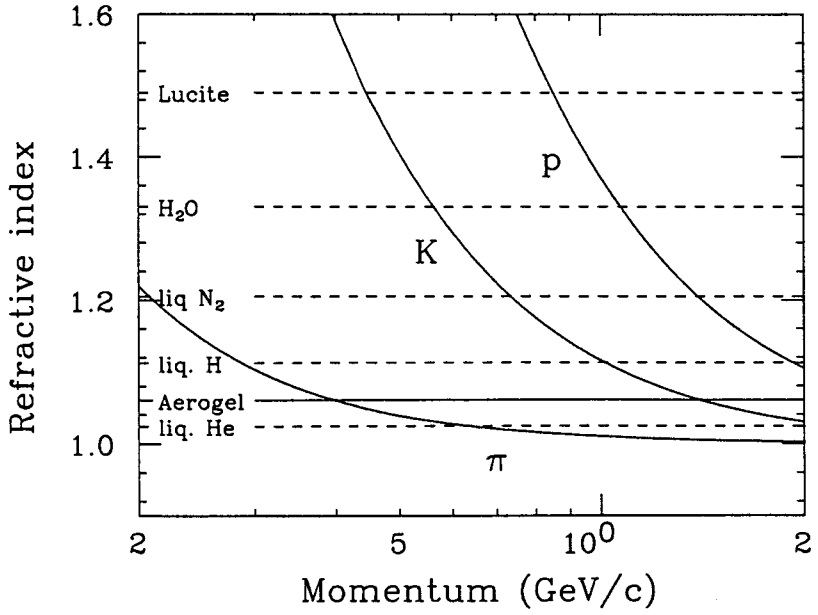

Figure 2.19: Threshold refractive index for Čerenkov radiation as a function of the momentum.

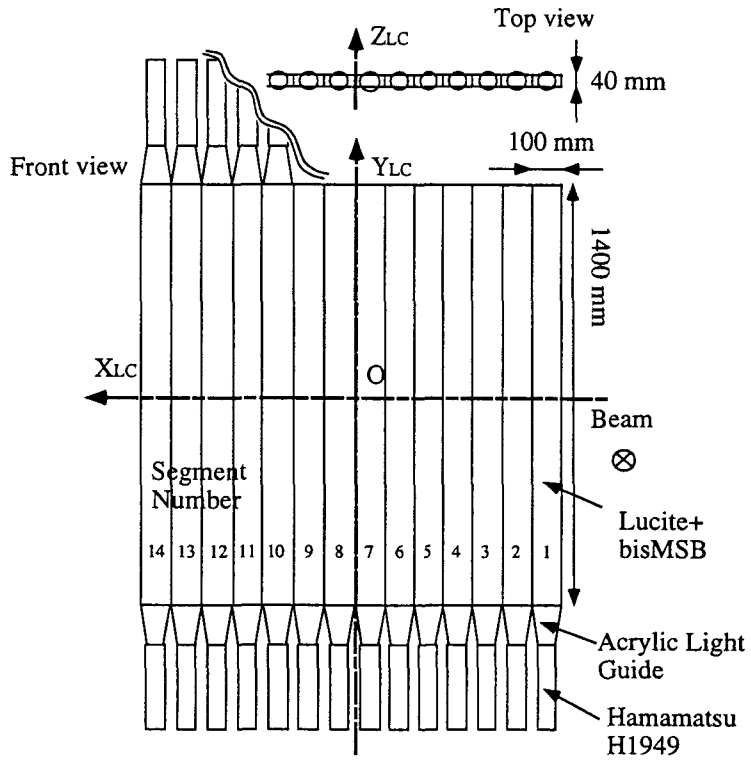

Figure 2.20: Schematic view of LC.

target. A differential type Lucite Čerenkov counter, BLC, was newly installed right after the target. The coincidence of two photomultiplier attached to the both ends of counter was used for rejection beam related events. Figure 2.21 shows a schematic view of the BLC counter. The critical angle for total reflection is $\theta_c = 42.15°$ which is suitable to discriminate π^+ and K^+ around 720 MeV/c as shown in Figure 2.22. To obtain uniform efficiency over the large acceptance of the SKS magnet, $-18° \sim 18°$, the counter was bended and the center of curvature was placed at the target. Since the dominant part of Čerenkov light is in UV region, UV transparent Lucite and photomutipliers were selected and silicon oil, KF96H-50M(Shin-etsu), was used to couple them. The transmission of the silicon oil is better than the other material such as optical cement or optical grease in UV region[41].

2.4 Decay counter systems

The decay counter systems were installed above and below the target symmetrically as shown in Figure 2.23. Each system consisted of Silicon Strip Detectors(SSD),

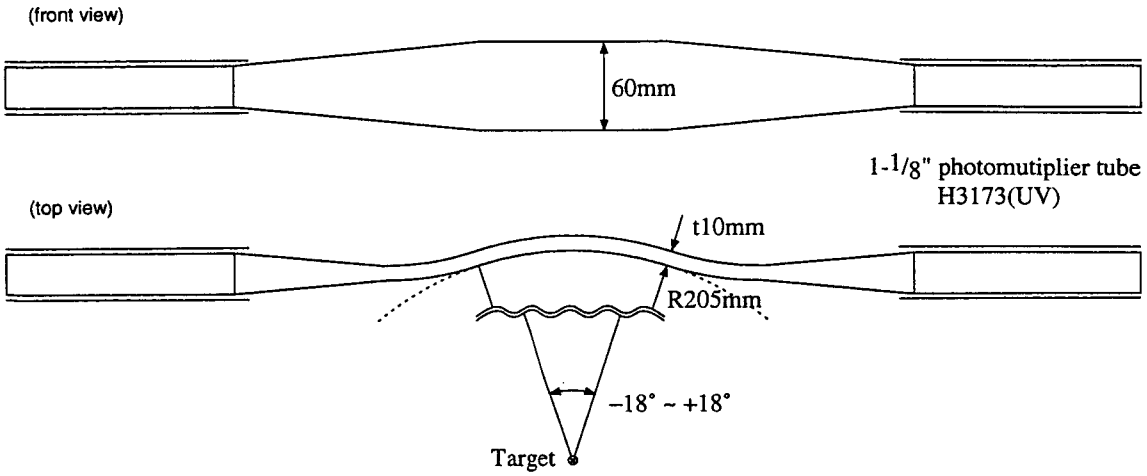

Figure 2.21: Schematic view of BLC.

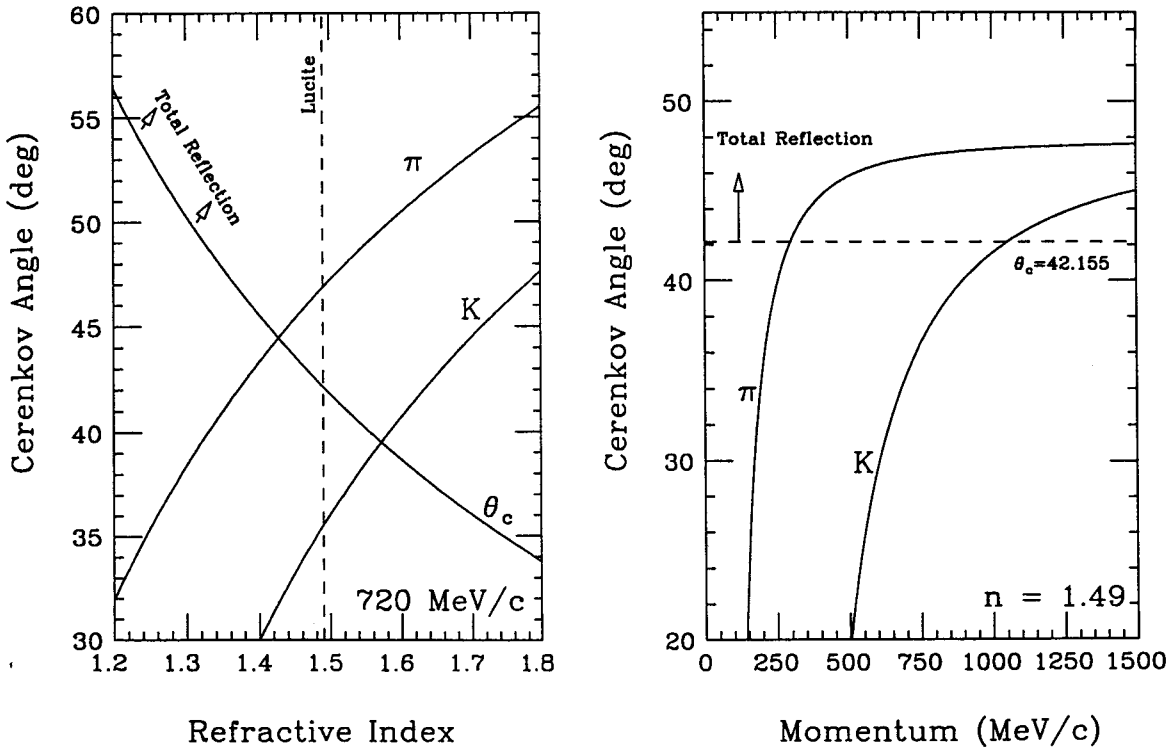

Figure 2.22: Čerenkov angle for π and K as a function of refractive index(left) and as a function of momentum(right). θ_c represents the critical angle for total reflection.

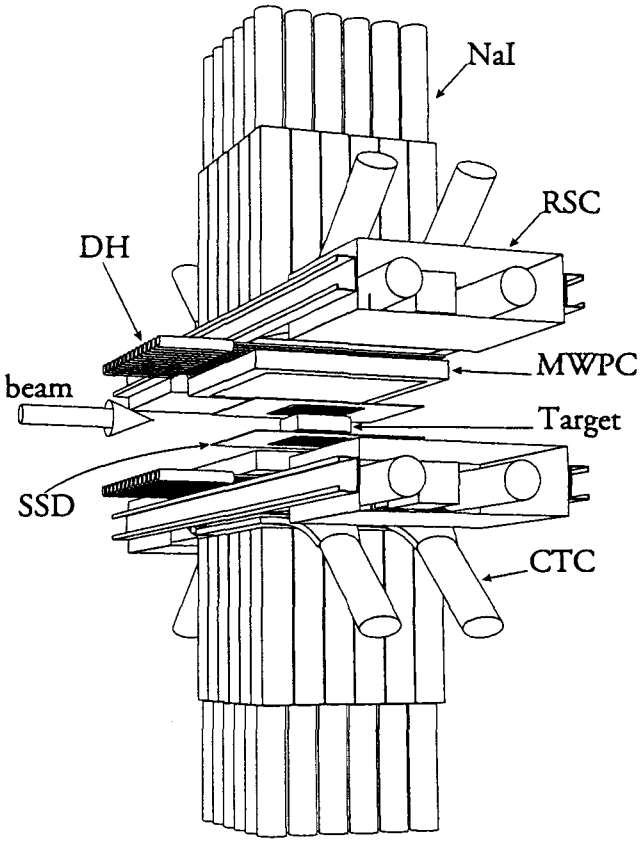

Figure 2.23: Schematic view of decay counter systems.

Name	Counter type/PMT	Coverage(cm)/Segmentation	Measurable
SSD	Silicon Detector	6.2(X)×6.2(Z)×0.05(T) 1 mm strip	ΔE, z-position
MWPC	Proportional Chamber	20(X)×20(Z)×3 layer 2 mm spacing	z, x, z-position
DH	Plastic H3165	21(X)×20(Z)×0.2(T) 14 segments	x-position
RSC	Plastic/Lead H1161, H4139	30(X)×30(Z)×38.4(T) 2 segments	total E, Range
CTC	Plastic H1161	40(X)×40(Z)×2(T) 2 segments	ΔE
NaI	NaI H1161	38(X)×38(Z)×30(T) 6×6 segments	E_γ

Table 2.8: Specifications of the elements of decay counter system.

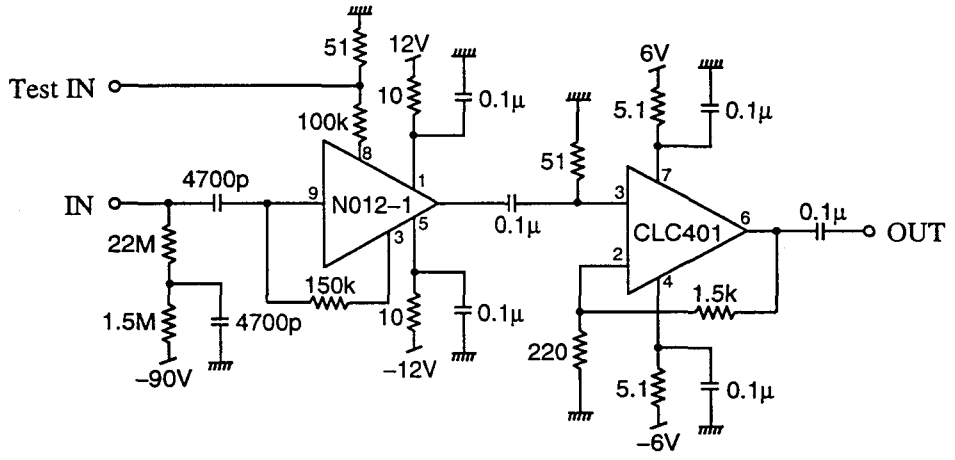

Figure 2.24: Schematic diagram of readout electronics for SSD.

MultiWire Proportional Chamber(MWPC), Range Shower Counter(RSC) and 36 NaI detectors and covered about 30% of the total solid angle. The energy loss information measured by SSD was used for identification of decay protons and pions with the total energy and the range information from RSC. The tracking information from SSD and MWPC was used for the correction of the path length in SSD and RSC. NaI detectors are used for π^0 detection. The specifications of each counter element are summarized in Table 2.8. Here x, y and z represent horizontal, vertical and beam direction, respectively.

The size of SSD were determined so as to cover the 99% enriched ^{6}Li target, which has the size of 40(X)×20(Y)×60(Z) mm^3. Figure 2.24 shows a schematic diagram of read-out electronics. The signal from 62 strips were read by ADC individually. The gain of the amplification was adjusted so that the full range of ADC corresponded to the energy deposit(ΔE) of 4 MeV.

Figure 2.25 shows a schematic view of MWPC. MWPC had three anode planes and four cathode planes. Each anode plane had 96 wires to measure z, x and z positions, in order from target side. The gap between the anode plane and the cathode plane was 4 mm. The anode wire were made of gold-plated tungsten($\phi 20\mu$m). The cathode planes were made of 12 μm carbonated alamid film. The gas mixture was Ar(90%)+CH_4(10%) at atmosphere pressure. The read-out electronics are schematically shown in Figure 2.26. The preamplifier module for the beam drift chambers was used, but SPIDER read-out system was used instead of amplifier/discriminator module and TDC(TKO Dr. T). The SPIDER system consisted of two part, SPIDER-NET and SEM. The signals from preamplifiers were amplified

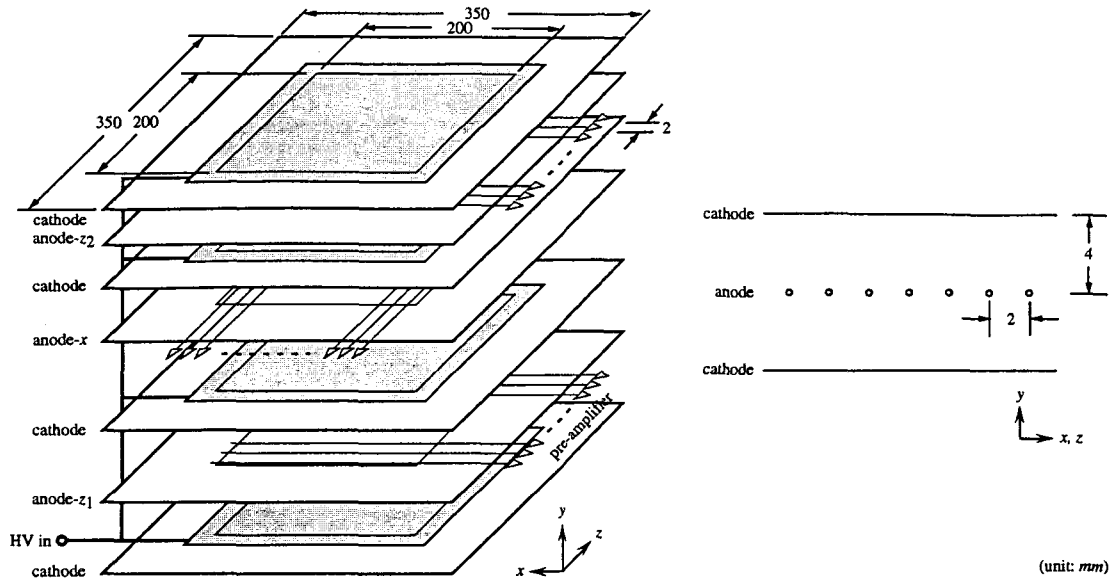

Figure 2.25: Schematic view of MWPC.

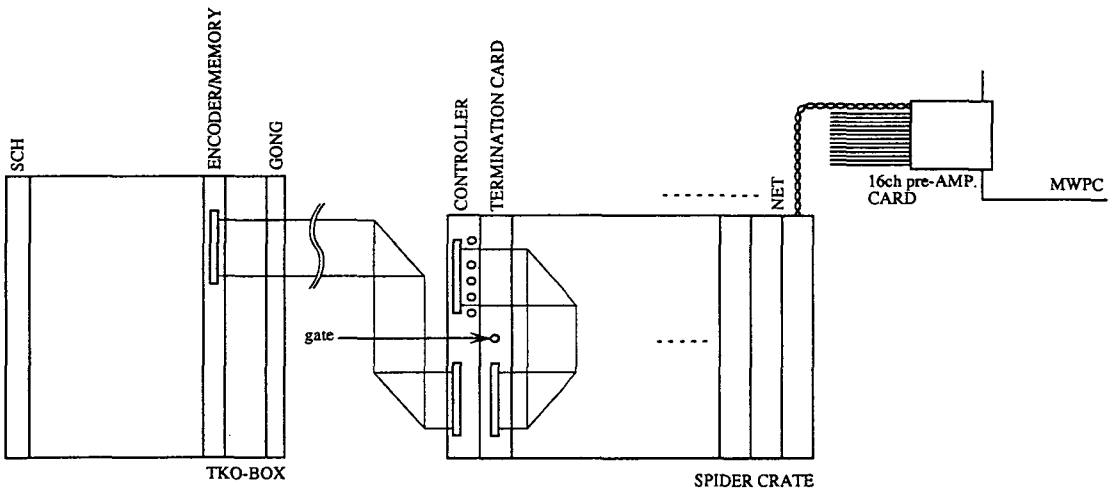

Figure 2.26: Readout system for MWPC.

and discriminated by SPIDER-NET. The channel ID's of the wire whose discriminated signal was in the gate provided by SEM were send and stored into SEM. The threshold for the discrimination were adjustable on SEM. Figure 2.27 show the efficiencies as a function of high voltage on cathode plane measured by π^+ beam at 500 MeV/c. Figure 2.28 shows the efficiencies as a function of gate timing measured on the (π^+, K^+) condition. The arrows in the figures are setting position.

DH was located next to the MWPC's. DH was divided into 14 segments to

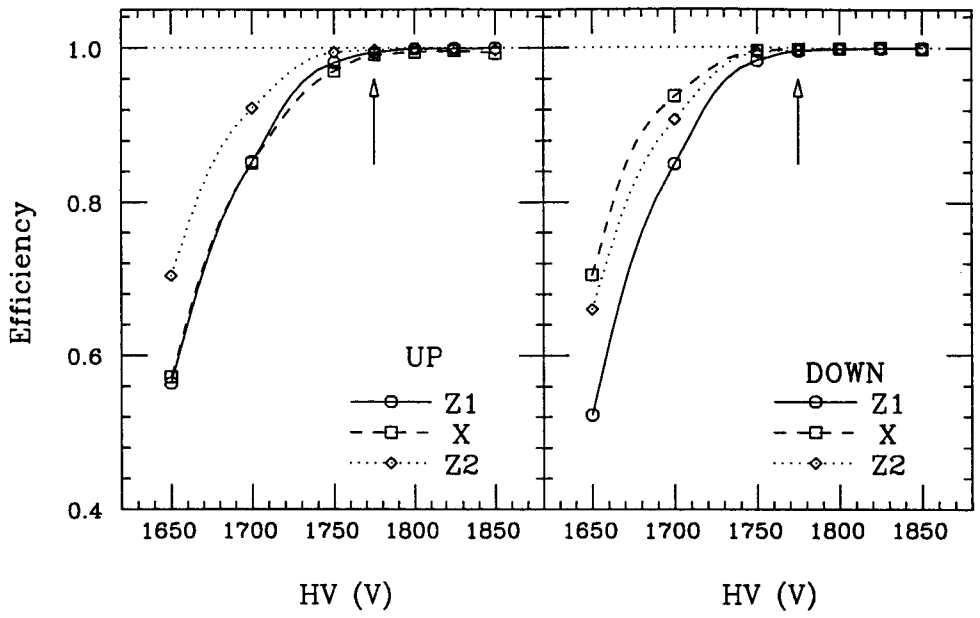

Figure 2.27: Efficiency as a function of high voltage on cathode plane measured by 500 MeV/c π^+.

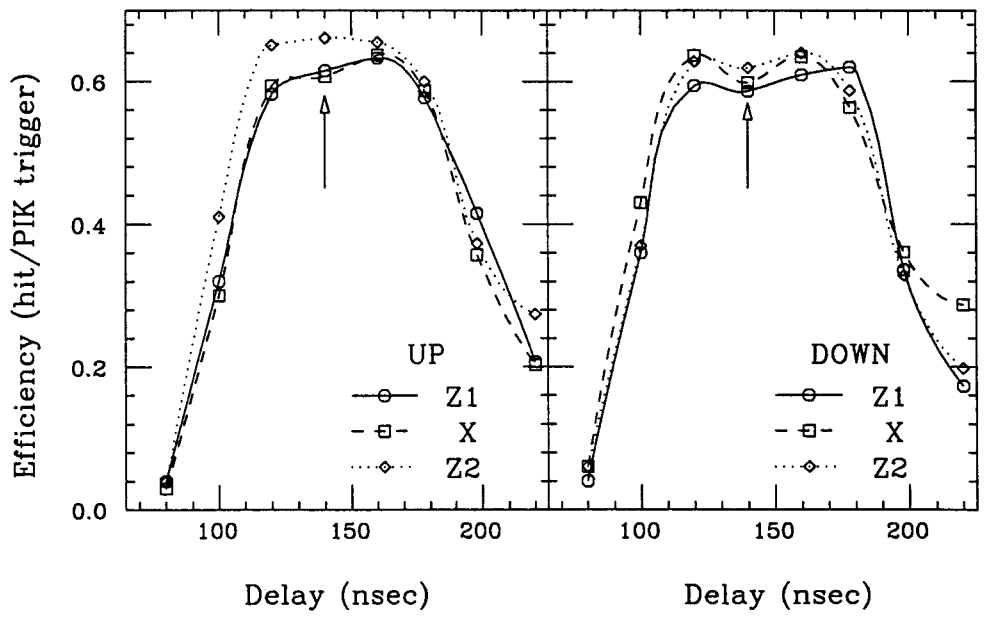

Figure 2.28: Efficiency as a function of gate timing supplied into SPIDER system on (π^+, K^+) condition.

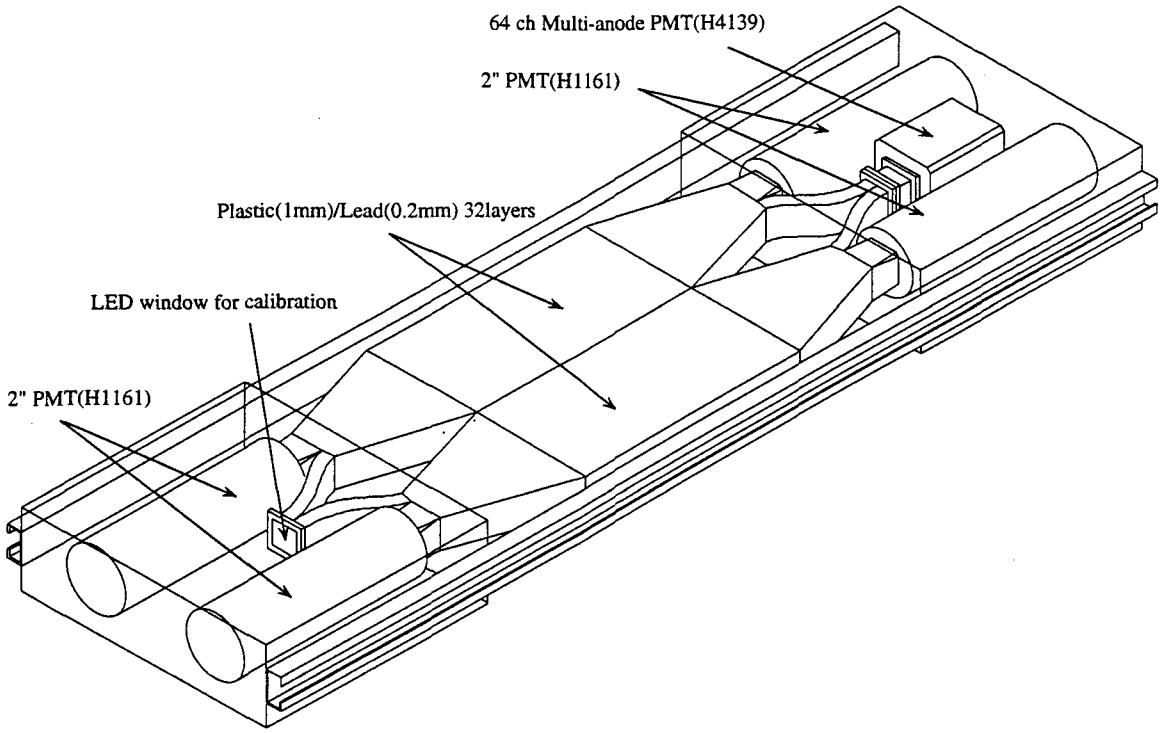

Figure 2.29: Schematic view of RSC.

provide coarse x position for tracking the decay particles. Each segment had a dimension of $1.5(x) \times 0.25(y) \times 25.0(z)$ cm^2. 1/2" photomultipliers were attached to the ends on upstream side, since there was no space on downstream side.

Figure 2.29 shows a schematic view of RSC. RSC, which had 32 layers of 0.2 mm lead/1 mm plastic scintillator sheets, provided the information of total energy(E) and range(R) of decay products. RSC was divided into two segments along z direction. Each segment covered 30(X)×15(Z) cm^2 area. The scintillation photon was read by 2" photomultiplier attached to the both ends of segments for E measurement and by 64 channel multi-anode photomultiplier through a fiber bundle attached to each plastic sheet individually for R measurement. Each fiber bundle consisted of sixteen 1×1 mm^2 optical fibers so as to fit a anode pad, which had a size of 4×4 mm^2.

CTC was the next counter of RSC. CTC was divided into two segments along z direction. The size of each segment was 30(x)×15(z)×1(t) cm^3. CTC was used for tagging the particles passing through RSC, whose range and energy were not able measured, and also used as a veto counter for NaI.

NaI array was installed most outside of the decay counter systems for decay π^0

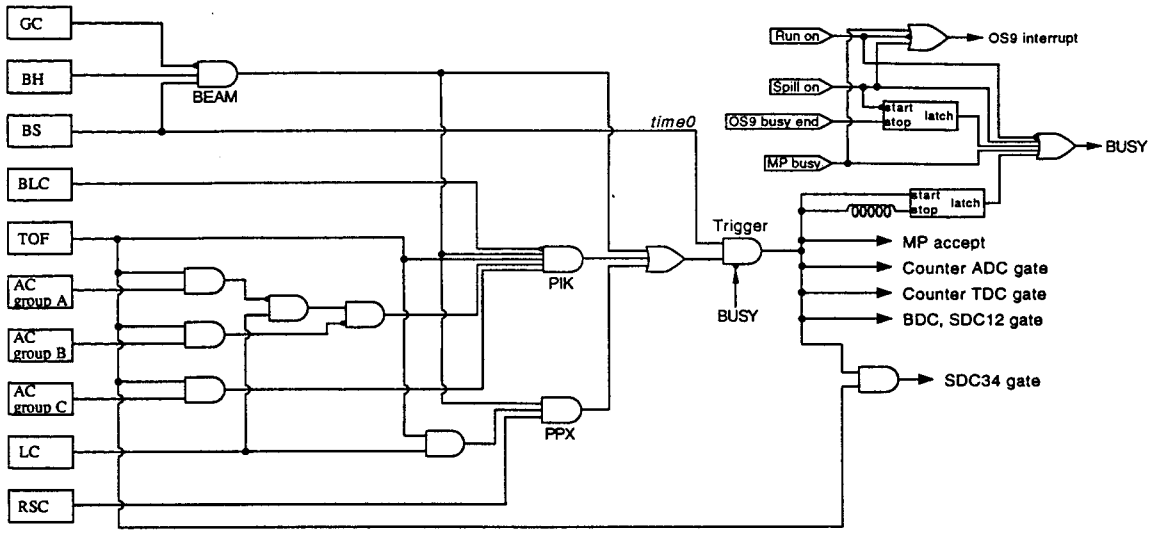

Figure 2.30: Trigger diagram.

detection. Each NaI array consisted of 6×6 segments whose seize was 6.5×6.5×30 $cm^3(L_R = 11.6)$. This thesis does not touch the analysis for NaI.

2.5 Trigger system

High intensity beam, as its rate of a few million per second, caused enormous background trigger via pion-nucleus reactions, such as $(\pi, \pi' X)$ and (π, pX) whose cross section are typically three orders of magnitude larger than that for the (π^+, K^+) reaction. Therefore a powerful trigger system was of vital importance for the experiment. In the present system, the (π^+, K^+) trigger comprised three kinds of trigger counters in the beam spectrometer(BH, BS and GC), and four kinds of trigger counters in SKS spectrometer(BLC, TOF, AC1-2 and LC), as mentioned in the previous sections.

Figure 2.30 shows a trigger diagram. The BEAM was defined by $\overline{\mathrm{GC}} \times \mathrm{BH} \times \mathrm{BS}$. Mean timer modules were used to remove the incident position dependence of the trigger timing for BH and BS. The proton contamination in the beam was rejected by a timing coincidence between BH and BS with a coincidence width of about 5 nsec. The time difference between pions and protons was about 10 nsec.

The (π^+, K^+) trigger(PIK) was defined by $\mathrm{BEAM} \times \overline{\mathrm{BLC}} \times \mathrm{TOF} \times \overline{\mathrm{AC1}} \times \overline{\mathrm{AC2}} \times$ LC. Mean timer modules were used to remove the incident position dependence of the trigger timing for TOF and LC. Besides of above two trigger $(\pi^+, \pi^{+\prime} X)$

Name	Definition	Rate/spill	Prescale Factor
BEAM	$\overline{GC} \times BH \times BS$	3.0×10^6	2×10^5
PIK	$BEAM \times \overline{BLC} \times TOF \times \overline{AC1} \times \overline{AC2} \times LC$	90	1
PPX	$BEAM \times TOF \times LC \times RSC$	45	70

Table 2.9: Definition of the on-line triggers. The typical rate per spill and prescale factor used for the data taking are also shown.

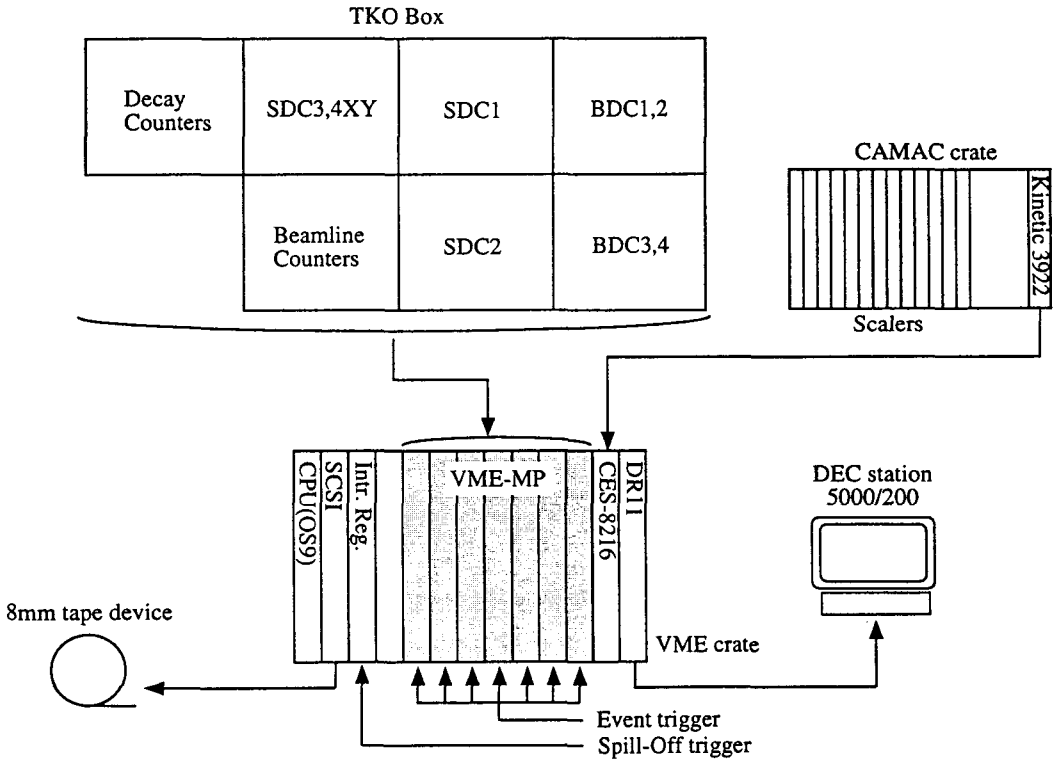

Figure 2.31: A diagram of the data-acquisition system.

trigger(PPX) was employed for monitoring a spurious asymmetry of decay counter systems. The trigger was defined by BEAM × TOF × LC × RSC.

The trigger timing was determined by BS. In order to avoid time jitter by several circuits modules, the BS signal was taken a coincidence again after the trigger logic was constructed as shown in the trigger diagram. It determined the gate timing of the TDC and ADC modules, except for SDC3, SDC4X and SDC4Y, for which the TOF timing determined the gate timing to avoid flight time difference in SKS.

In the normal run condition, PIK trigger and prescaled BEAM and PPX triggers were taken simultaneously. Typical trigger rates are summarized in Table 2.9.

2.6 Data acquisition system

Figure 2.31 shows a diagram of the data acquisition system. First, event by event, raw data were fed into the TDC and ADC modules of the KEK-TKO standard[42]. Their digitized data were then stored in VME memory modules(MP). During a spill-off period, those accumulated data were written on an 8mm tape device after being processed by a CPU module where OS9 operating system was running. A CAMAC crate is also connected to the system to handle scaler data spill by spill. A typical data size was about 600 long words per event after zero-suppressing. A typical dead time was 3% for a trigger rate of 150 counts/spill. For online monitoring, the raw data were transferred to a workstation through a DR11 module. The data acquisition task in VME was independent of the data monitoring tasks in the workstation.

2.7 Data summary

The data were taken for two enriched(95%) ^{6}Li targets whose thicknesses were 2.77 g/cm^2 and 1.24 g/cm^2. The thinner target were used to check the excitation energy spectrum of $^6_\Lambda$Li produced by the ^{6}Li(π^+, K^+) reaction, since the effect of the multiple scattering and the energy loss struggling in the target was less than the thick target. Total number of beam particles is listed in Table 2.10 for two targets.

Target	Thickness (g/cm^2)	Number of beam π^+	PIK trigger
^{6}Li	2.77	9.28×10^{11}	2.66×10^7
(95% enriched)	1.24	1.07×10^{11}	1.74×10^7

Table 2.10: Data summary.

Chapter 3

Analysis

In this chapter, procedures of data analysis from the raw data are described. The analysis stage is divided into two parts: a (π^+, K^+) reaction part and a decay particle part.

The hypernuclear mass(M_H) was calculated by a kinematical relation of the (π^+, K^+) reaction,

$$M_H = \sqrt{(E_\pi + M_A - E_K)^2 - (p_\pi^2 + p_K^2 - 2p_\pi p_K \cos\theta)}, \tag{3.1}$$

where M_A is the ^{6}Li target nuclear mass, θ is the scattering angle, and p_π, p_K, E_π and E_K are the momentum and energy of π^+ and K^+, respectively. Thus the variables, p_π, p_K and θ, had to be measured experimentally. Sections 3.1, 3.2 and 3.3 give the procedures to determine these three variables. Since the obtained raw data included a number of background events, event selection was playing important role to reduce background level. Section 3.4 describes the procedure of the event selection.

The present decay counter systems were sensitive to π^-, p and π^0 coming from three decay modes of hypernuclei,

$$\Lambda \rightarrow \boldsymbol{p} + \boldsymbol{\pi^-}, \tag{3.2}$$

$$\Lambda \rightarrow n + \boldsymbol{\pi^0}, \tag{3.3}$$

$$\Lambda + p \rightarrow n + \boldsymbol{p}. \tag{3.4}$$

In order to derive the asymmetry of each decay mode, decay particles had to be well identified. In section 3.5, decay particle identification using the present decay counter systems is described.

3.1 Momentum of a beam particle

The beam momentum was calculated from beam drift chamber data as follows. At first, straight tracks were defined locally at the entrance of QQDQQ by BDC1 and BDC2 and at the exit by BDC3 and BDC4 using least square method. For a multi-hit event, all possible combinations were examined. Next, the tracks at the entrance and exit of the QQDQQ were connected using a third order transport matrix which was calculated by ORBIT[43]. The particle's momentum(p_{K6}) was determined by least square fitting with a chi-square defined as

$$\chi^2_{K6} \equiv \frac{1}{N_{hit}-5}\left\{\sum_{\substack{i=1\\(\text{if hit})}}^{12}\left(\frac{P_i - f_i(\vec{X}_{in})}{w_i}\right)^2 + \sum_{\substack{i=13\\(\text{if hit})}}^{24}\left(\frac{P_i - g_i(\vec{X}_{out})}{w_i}\right)^2\right\}, \quad (3.5)$$

$$\vec{X}_{out} = \mathcal{M}(\vec{X}_{in}, \delta), \quad (3.6)$$

where P_i and w_i denote the hit position and resolution of the i-th plane(1–6 for BDC1 and so on) and N_{hit} represents the number of hit. The position for the trajectory at the i-th plane is denoted by $f_i(\vec{X}_{in})$ and $g_i(\vec{X}_{out})$. $\vec{X}_{in}$ and $\vec{X}_{out}$ represent the horizontal and vertical positions and their derivatives at the reference point for the transport matrix(x, y, dx/dz and dy/dz). $\vec{X}_{out}$ was calculated using the transport matrix($\mathcal{M}$), momentum of particle($\delta \equiv p/p_0$) and $\vec{X}_{in}$. A typical χ^2_{K6} distribution is shown in Figure 3.1. The event whose χ^2_{K6} was equal or less than 20 were accepted.

3.2 Momentum of a scattered particle

The momentum of a scattered particle was calculated from the SDC data as follows. At first, tracks at the entrance and exit of the dipole were defined locally by SDC1·2 and SDC3·4. For the SDC2, TDC information was not used and only the position of hit wires were used to find out the track. Since the SDC was tilted 30° along to the beam axis, it is difficult to calibrate the relation between the drift length and drift time. For SDC1 and SDC2 tracking, the effect of the magnetic field on the trajectory was taken account by hit-position shifts of about 2 mm from a straight track. For multi-hit events, all possible combination were examined. The consistency with the position of the TOF and LC hit segments was examined in defining the track at SDC3 and SDC4.

Next, the momentum was determined from those hit positions by reconstructing trajectory. The trajectory was reconstructed by the Runge-Kutta method[39] using

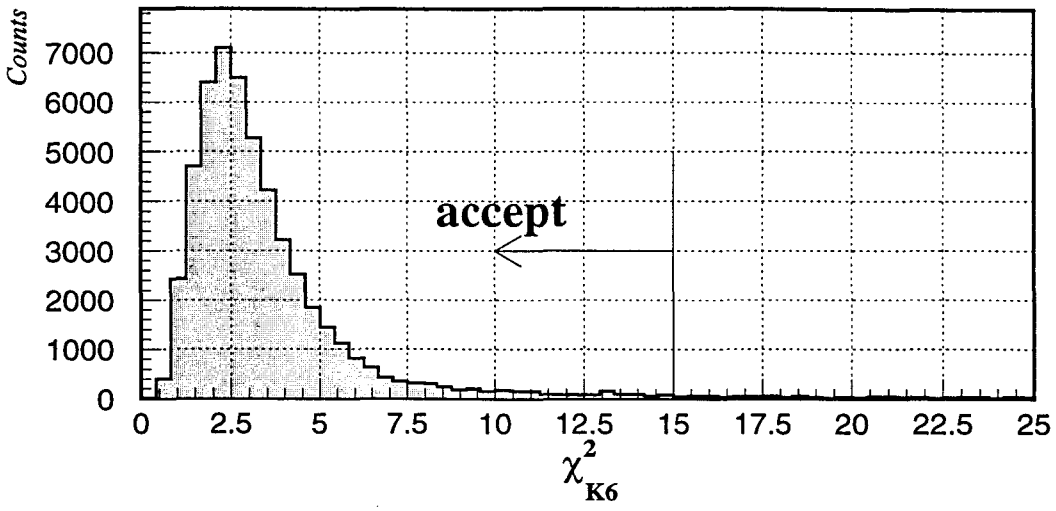

Figure 3.1: Typical distribution of χ^2_{K6} for (π^+, K^+) data. The arrow represents a cut point.

a measured magnetic field map[44]. In this method, the the chi-square defined below was minimized by iteration to optimize five parameters: the momentum and four independent variables concerning to the trajectory at the target. The chi-square(χ^2_{SKS}) is defined by

$$\chi^2_{SKS} = \frac{1}{N_{hit} - 5} \sum_{i=1}^{N_{hit}} \left(\frac{x_i^{tracking} - x_i^{data}}{w_i} \right)^2 , \tag{3.7}$$

where N_{hit} is the number of chamber planes having hits, $x_i^{tracking}$ and x_i^{data} are the hit positions on the i-th hit plane in the tracking and the data, respectively, and w_i is the position resolution of the i-th hit plane. The iteration was terminated either when the variation of χ^2_{SKS} was less than 10^{-3}, when the number of iteration reached 200 or when the χ^2_{SKS} reached 10^{10}. Figure 3.2 shows a typical χ^2_{SKS} distribution for (π^+, K^+) data. The event whose χ^2_{SKS} was equal or less than 25 were accepted.

3.3 Scattering angle

The scattering angle was determined by two tracks respectively defined in BDC3·4 and SKS tracking. Figure 3.3 shows typical horizontal and vertical scattering angle resolution; they are 3.3 and 5.6 mrad in rms, respectively. Because of the special wire configuration of the drift chambers, the vertical resolution was worse than the horizontal one.

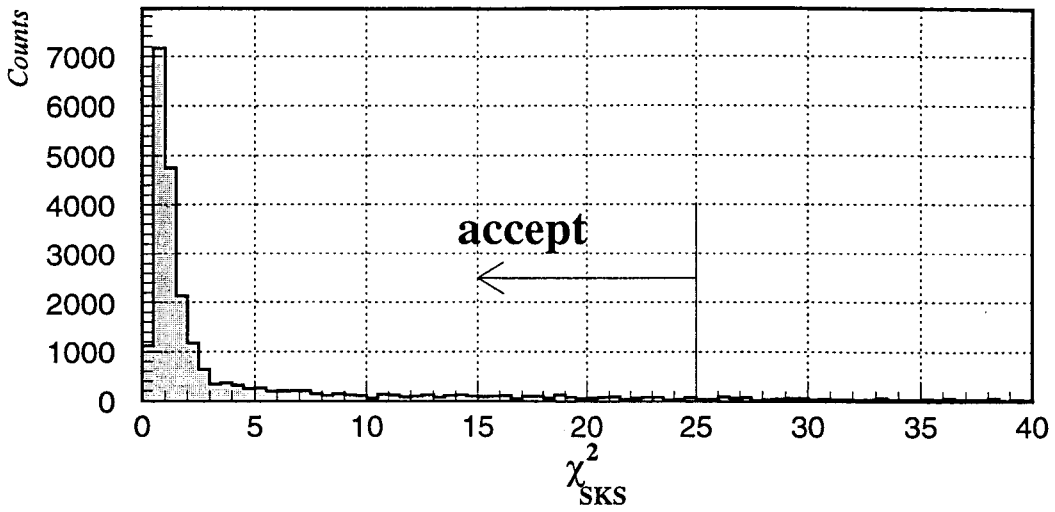

Figure 3.2: Typical distribution of χ^2_{SKS} for (π^+, K^+) data. The arrow represents a cut point.

The scattering angle resolution was important for rejecting background events associated with beam particles scattered into very forward angles. Figure 3.4 shows dx/dz of the tracks obtained in BDC3·4 and SDC1·2 for all (π^+, K^+) events. A large peak in the figure corresponds to the beam events. To minimize computation time the track candidates whose dx/dz were same with that of BDC3·4 track candidates were rejected before tracking whole SKS spectrometer.

3.4 Event selection

Background particles other than K^+ could be separated by TDC, ADC information from TOF and LC. Figure 3.5 show two dimensional scatter plots of TDC and ADC for TOF and LC. Boxes in the figures represent for the event selection at the first stage of data analysis in order to save computation time. After these selection the background events were reduced with a factor 10 as shown in Figure 3.6. Here the scattered particle mass(M_{sca}) was calculated using

$$M_{sca} = \frac{p}{\beta}\sqrt{1-\beta^2}, \tag{3.8}$$

$$\beta = \frac{L}{c\Delta t}, \tag{3.9}$$

where p is the momentum determined by SKS tracking, β is the velocity determined by the time-of-flight(Δt) and flight length(L) between BS and TOF wall obtained

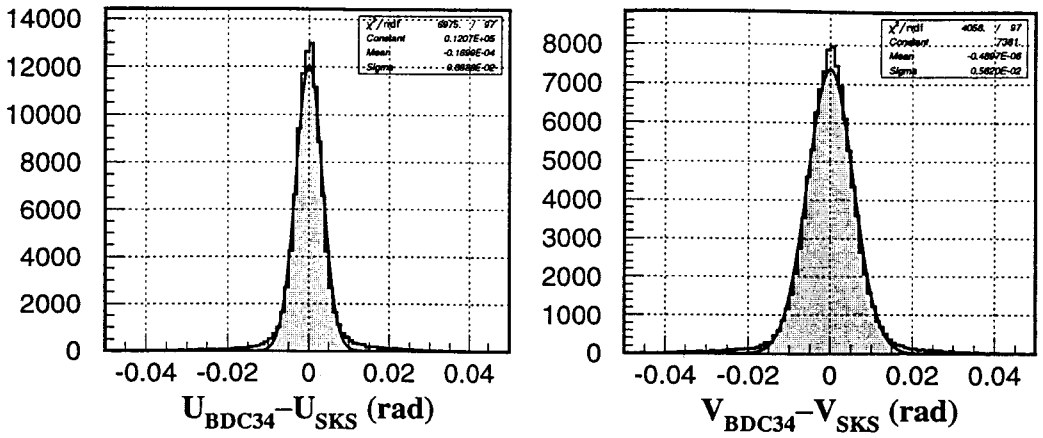

Figure 3.3: Typical distributions of the horizontal(left) and vertical(right) scattering angles measured by BDC3·4 and SKS tracking for 720 MeV/c π^+ beam trough data.

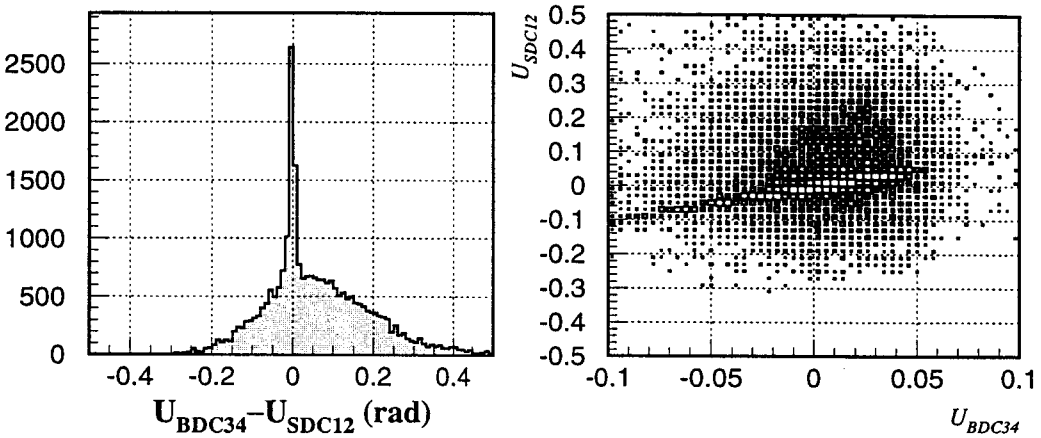

Figure 3.4: Difference of dx/dz between BDC1·2 and SDC1·2 track candidates for all (π^+, K^+) events.

from TDC information of each counter and the SKS tracking, respectively.

A vertex position of the reaction was used to identify the event which had a reaction in the target. The tracks obtained from BDC3·4 and SKS tracking were used to determine the vertex position where the distance of the closest approach(DCA) of each track were minimum. Figure 3.7 shows the distribution of vertex position for (π^+, K^+) data. In addition to the target, BS and BLC are shown in the z vertex distribution(Z_{VTX}). The large tails came from forward events, as shown

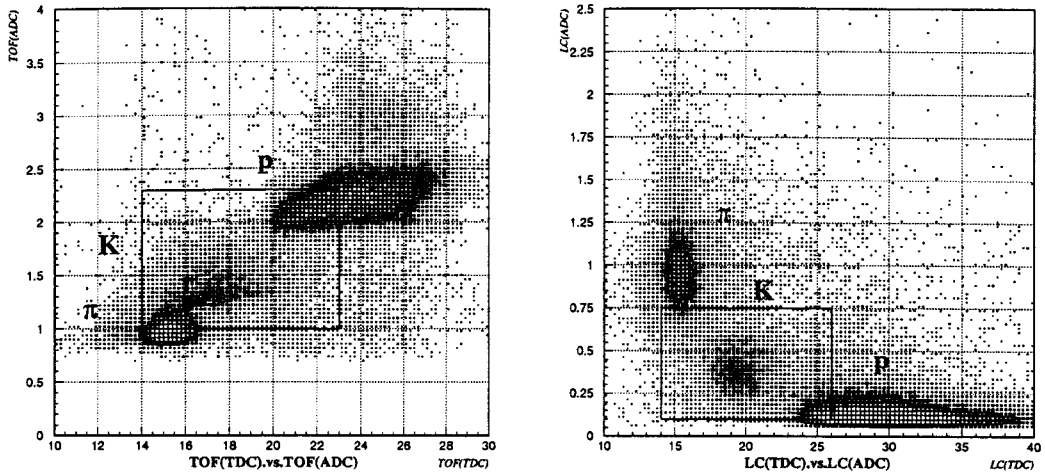

Figure 3.5: Two dimensional scatter plots between TDC and ADC for TOF(left) and LC(right).

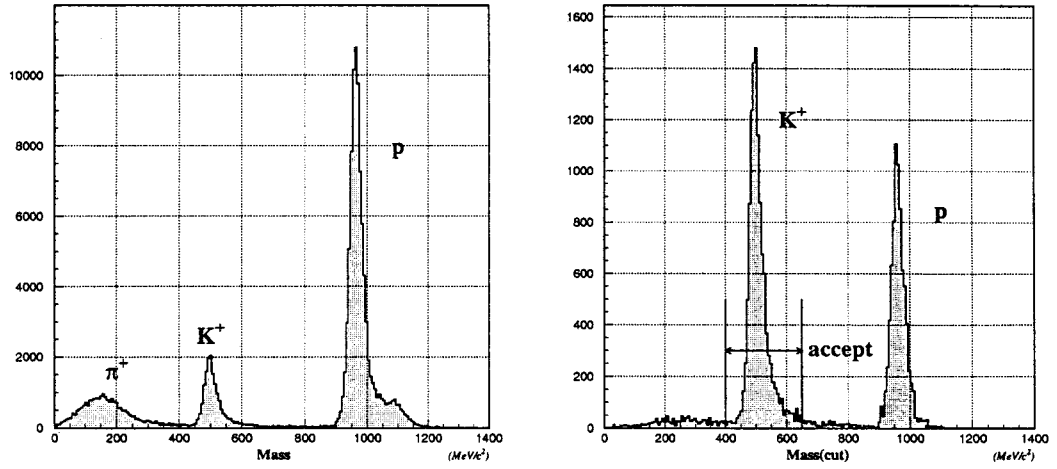

Figure 3.6: Scattered particle mass spectra for (π^+, K^+) data without(left) and with(right) ADC-TDC cut on TOF and LC.

in Figure 3.8, because the Z_{VTX} resolution was worse for the forward scattering angle. Arrows in Figure 3.7 represent the cut point for event selection. Furthermore the cut on DCA was applied to select the track candidates of beam and scattered particle(Figure 3.9).

The cuts used to select (π^+, K^+) event are:

1 ADC and TDC information from TOF and LC:

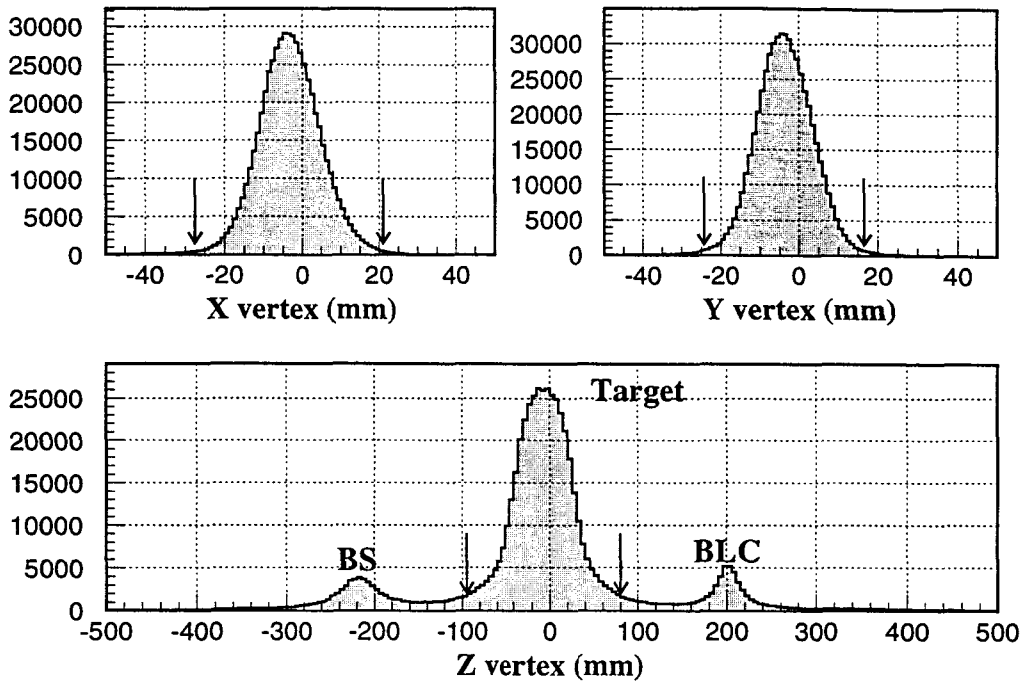

Figure 3.7: Distribution of x(Top-Left), y(Top-Right) and z(Bottom) vertex for (π^+, K^+) data. Arrows represent cut points.

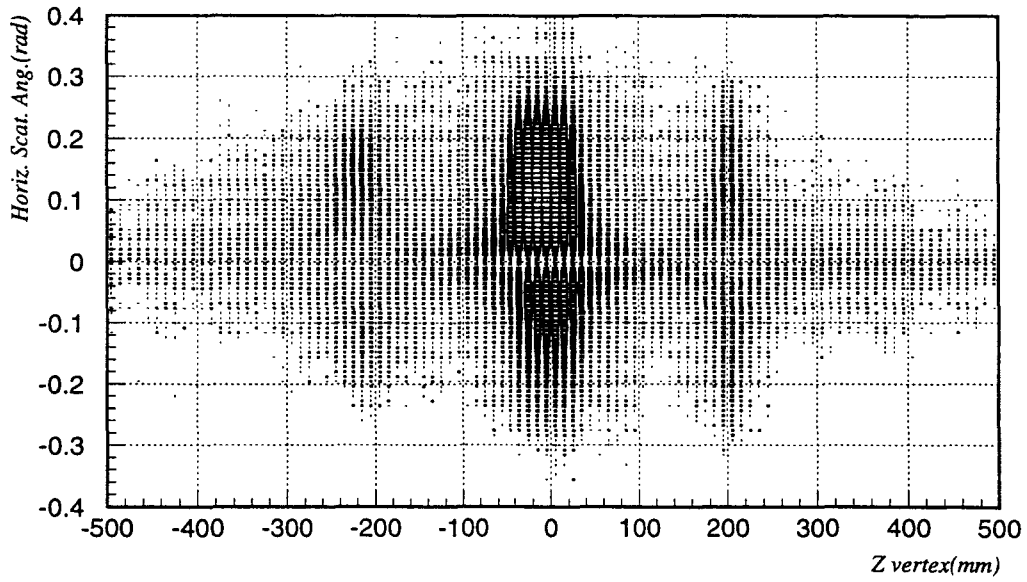

Figure 3.8: Two dimensional scatter plot between z vertex and horizontal scattering angle for (π^+, K^+) data.

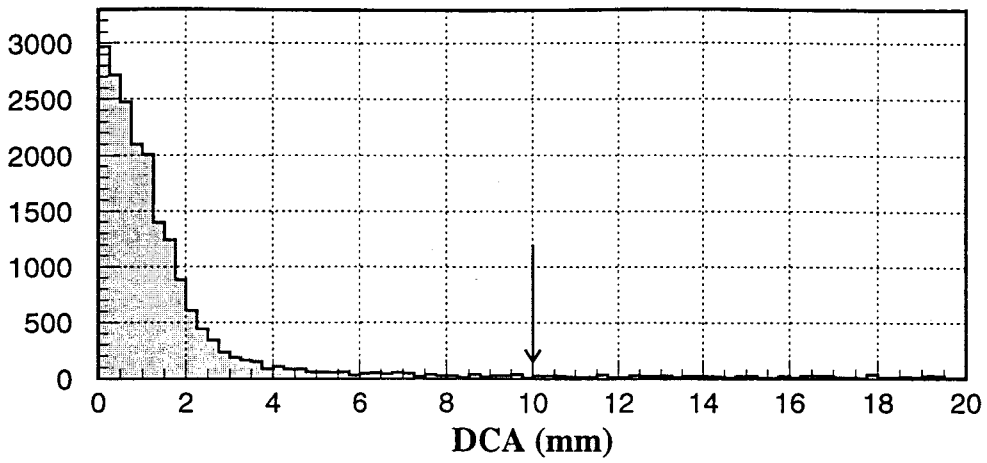

Figure 3.9: Distance of the closest approach between the tracks of beam and scattered particle. The arrow represents the cut point.

- $1.0 < \mathrm{TOF(ADC)} < 2.3$
- $14.0 < \mathrm{TOF(TDC)} < 23.0$ nsec
- $0.1 < \mathrm{LC(ADC)} < 0.75$
- $14 < \mathrm{LC(TDC)} < 26$ nsec

Each ADC were calibrated as that the pion peak was equal to 1.0.

2 Time-of-flight between BH and BS(see Figure 2.11):

- $-1.5 < \Delta T_{BH-BS} < 1.5$ nsec

3 Difference between dx/dz's of the tracks defined by BDC3·4 and SDC1·2:

- $|(dx/dz)_{BDC34} - (dx/dz)_{SDC12}| > 10$ mrad

for all the combinations of track candidates

4 Chi-squares of QQDQQ and SKS tracking:

- $\chi^2_{K6} < 15$
- $\chi^2_{SKS} < 25$

5 Scattering particle mass:

- $400 < M_{sca} < 650$ MeV/c^2

6 Reaction vertex(X_{VTX}, Y_{VTX} and Z_{VTX}):

- $-27.5 < X_{VTX} < 21.0$ mm
- $-24.3 < Y_{VTX} < 16.5$ mm
- $-95.0 < Z_{VTX} < 80.0$ mm

7 Distance of the closest approach(DCA) between two tracks defined by BDC3·4 and SKS tracking:

- $DCA < 6$ mm

3.5 Decay particle identification

3.5.1 Energy calibration

All the elements of the decay counter systems were calibrated by the cosmic ray data. Figures 3.10 to 3.13 show the measured energy deposit on each counter. Solid lines in the figures indicate the results of the GEANT simulation for 4 GeV μ^+ particles as the cosmic ray. For the full simulation for the decay counter systems later, saturation effects for highly ionizing particles were included for scintillators with Birk's law[45].

SSD

The energy resolution of SSD is mainly determined by electrical noise and Landau fluctuation since the thickness of SSD was 500 μm. After the correction for path length, we obtained the resolution of 58 keV at FWHM. The electrical noise was 42 keV derived by the width of pedestal and the effect of the Landau fluctuation is estimated as 43 keV for the cosmic ray. The simulation which includes constant energy resolution of 42 keV reproduces the measured ADC spectrum for the cosmic ray. The threshold energy was set to 60 keV.

DH

Figures 3.11 show a pulse height distribution for cosmic ray and its position dependency as a function of z position measured by MWPC and SSD. This position dependence was corrected by exponential curve as a solid curve in the figure. The width of a cosmic ray peak is 0.16 MeV at FWHM while the mean energy deposit is 0.42 MeV. In the simulation, the resolution was included as $15.3(\%)/\sqrt{\Delta E(\mathrm{MeV})}$.

RSC

The energy deposit in RSC is obtained as

$$C\sqrt{\mathrm{ADC_{right}} \cdot \mathrm{ADC_{left}}}, \tag{3.10}$$

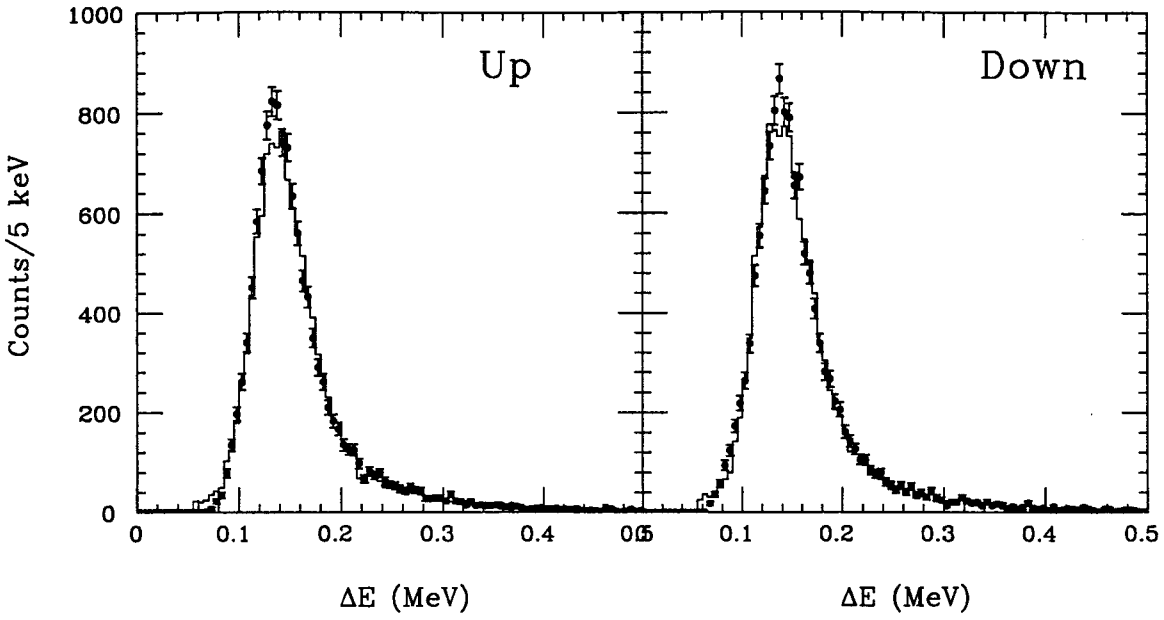

Figure 3.10: ADC spectrum of SSD for cosmic ray.

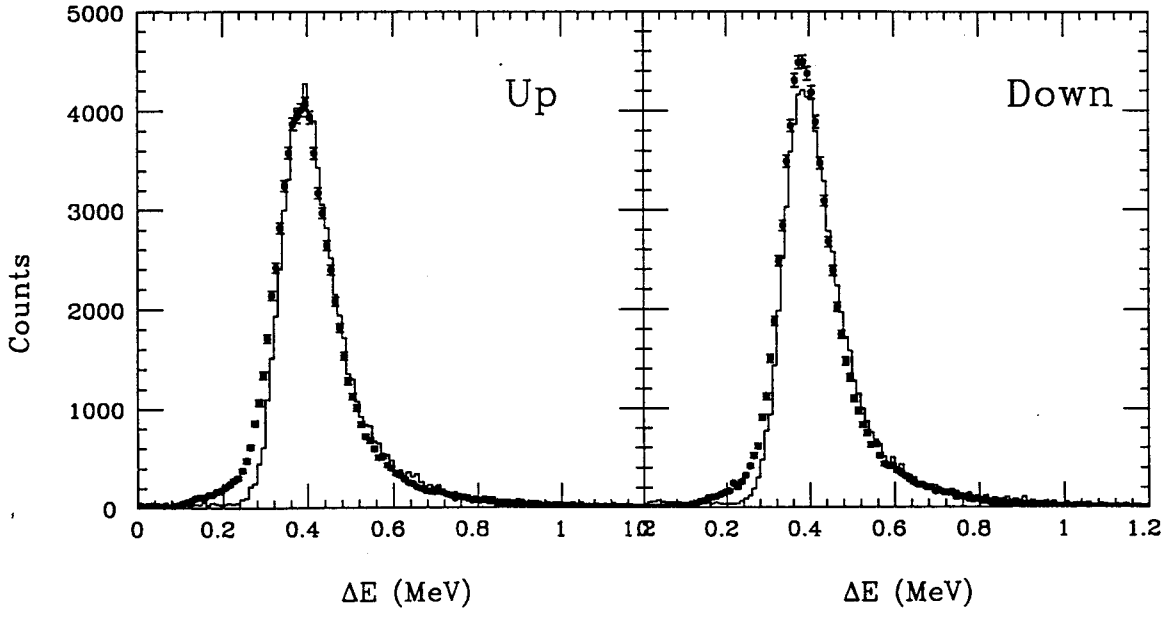

Figure 3.11: ADC spectrum of DH for cosmic ray.

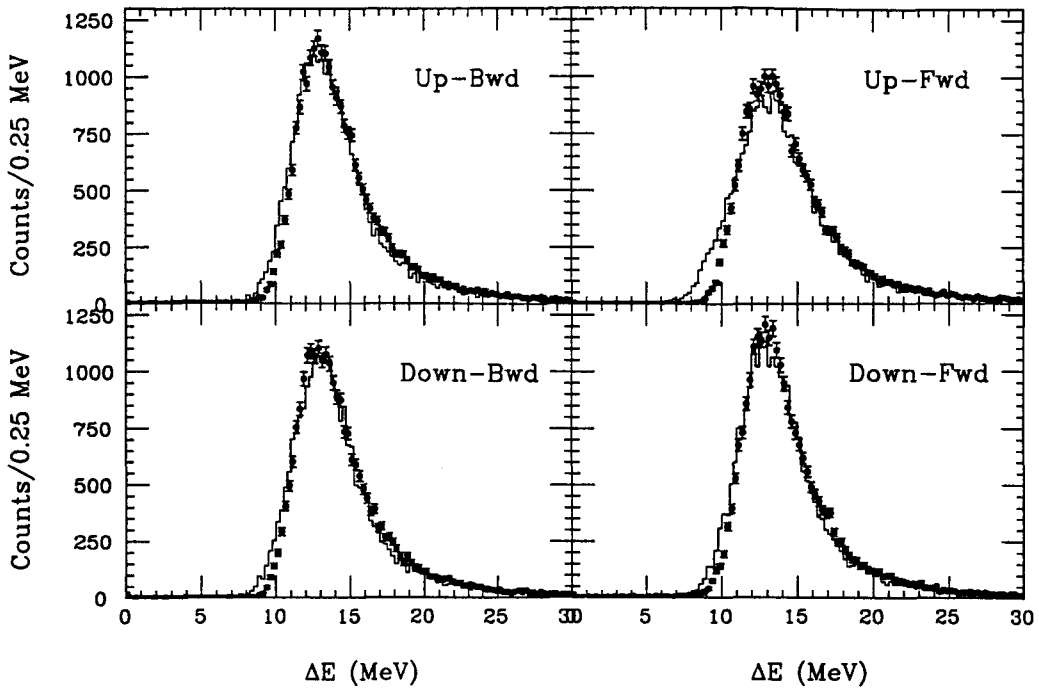

Figure 3.12: ADC spectrum of RSC for cosmic ray.

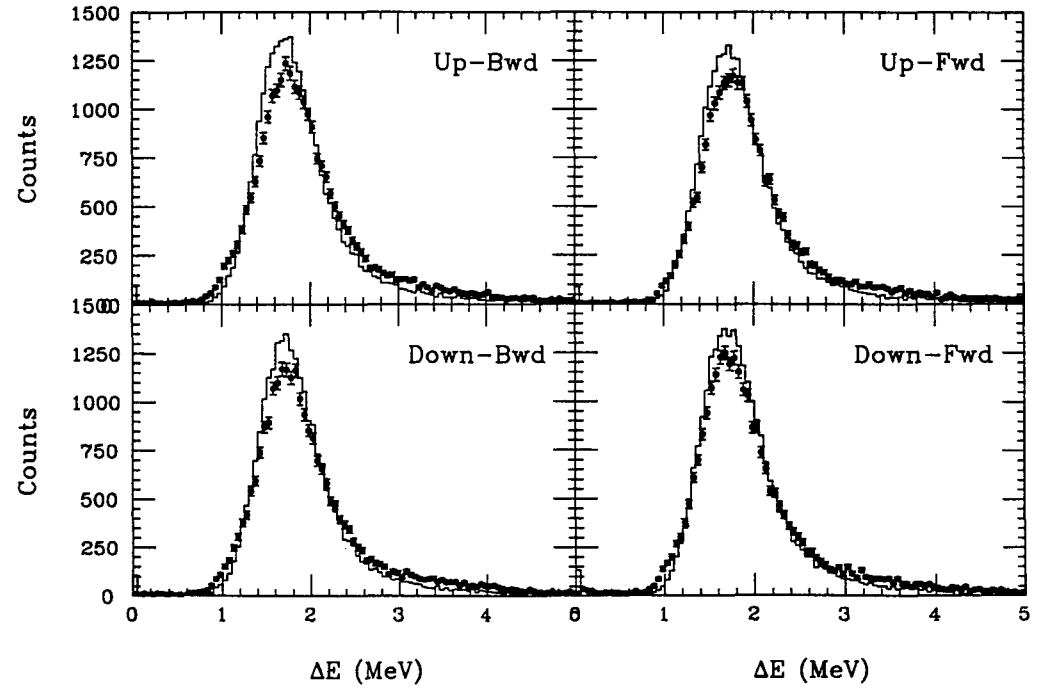

Figure 3.13: ADC spectrum of CTC for cosmic ray.

where the $\mathrm{ADC}_{(\mathrm{right,left})}$ and C are the pulse heights of the phototubes on each end of RSC measured by ADC, and coefficient for gain adjustment . The obtained energy deposit has no position dependence along the z direction as well as the x direction, although the light collection is not symmetric along the z direction as shown in Figure 2.29. The resolution of RSC for the cosmic ray is 4.6 $\sim$ 5.9 MeV at FWHM with the correction for the path length in RSC. In the simulation, the resolution was included as $\sigma(\%)/\sqrt{\Delta E(\mathrm{MeV})}$. The σ was 29.3, 35.6, 30.4 and 31.5 % for each segment.

CTC

The CTC is the last counter for the charged particles, p and π^-, from hypernuclear decays. Figure 3.13 shows the energy deposit distribution on CTC for cosmic ray. The width of the peak is 0.9 MeV at FWHM. In the simulation, the resolution was included as $53.0(\%)/\sqrt{\Delta E(\mathrm{MeV})}$.

3.5.2 Decay particle tracking

In order to obtain good resolution of particle identification, we measured the tracks of the particles and corrected the energy deposit on SSD. In the analysis, tracks were defined in $x-y$ and $z-y$ planes independently. The vertex of the (π^+, K^+) reaction, the x plane of MWPC and DH were used to find out the tracks in $x-y$ plane. SSD and two z planes of MWPC were used to find out the tracks in $z-y$ plane. The method of least squares was employed and for the multiple hit events all the candidates were tested and the minimum chi-square track was accepted. To reduce background tracks, we required the tracks crossing RSC segment whose pulseheight was above 5 MeV.

3.5.3 Particle Identification

The energy loss dE/dx in the medium is given by Bethe's formula[46] as,

$$\frac{dE}{dx} \propto \left(\frac{Z_{inc}}{\beta}\right)^2 \left[\log\left(\frac{2m_e\beta^2}{I(1-\beta^2)}\right) - \beta^2 - \frac{\delta}{2} - \frac{C}{Z_{med}}\right], \tag{3.11}$$

where Z_{med}, Z_{inc} and β are the atomic number of medium, the charge number and the velocity of the incident particle. I is equal to the logarithmic mean ionization potential of the medium, which is usually given as a parameter. C/Z_{med} and $\delta/2$ are the well known corrections accounting for the inner shell electron effect and the

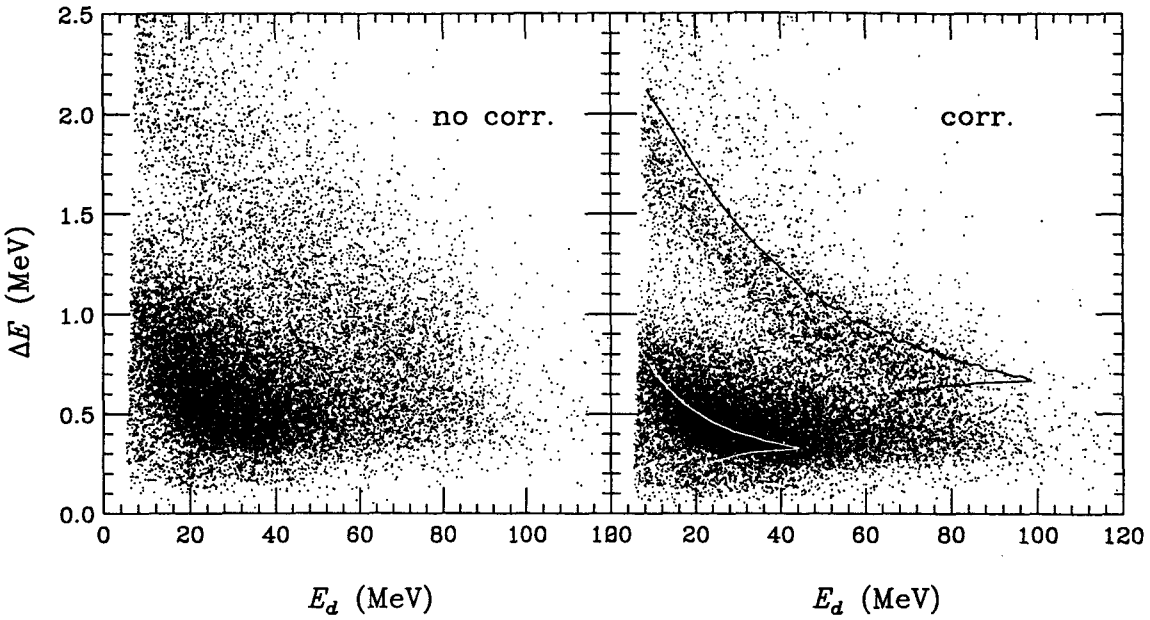

Figure 3.14: Two dimensional plot of the total energy(E_d) versus the energy deposit on SSD(ΔE) for the (π^+, K^+) data(left). The same plot using energy deposit on SSD with path length correction(right). The solid line indicates the Bethe-Bloch calculation.

density effect. The velocity β is related with the kinetic energy(E) as,

$$\beta = \frac{p}{E+m} = \frac{\sqrt{(E+m)^2 - m^2}}{E+m}. \tag{3.12}$$

Therefore there is clear correlation between the mass and the dE/dx for the charged particles(with energies below the minimum ionizing energy) and this correlation can be used to identify the particles.

Figure 3.14(left) shows the two dimensional plot of total energy(E_d) versus the energy deposit on SSD(ΔE). The E_d was the sum of the pulse heights of SSD, RSC, CTC and the pulse heights were calibrated by cosmic ray as mentioned in Section 3.5.1. DH was not used for the E_d because of its non-linear response for large energy deposit. Two loci corresponding to the protons and the pions are shown. Once the path length correction was applied on ΔE by tracking the decay particles, the loci were sharpened as in Figure 3.14(right). The solid line in the Figure 3.14(right) indicates the prediction for the E_d by Eq. 3.11 with the measured ΔE. The discrepancy is mainly due to the attenuation of the pulseheight of RSC for large local energy deposit. Besides more, in low energy region, the materials between

SSD and RSC such as the wrapping film for counters reduced measured total energy. In the following analysis on particle identification, we added the $t_{inv}\Delta E$ on E_d to take into account the invisible energy deposit in DH and the other materials. t_{inv} is the parameter and depends on the thickness of the material.

In order to separate the pions and the protons, PI(particle identification) function was defined as

$$F_{E\Delta E} \equiv F_{E\Delta E}(E_d, \Delta E) = \alpha \log(E_d + t_{inv}\Delta E) + \beta \log \Delta E + \gamma, \tag{3.13}$$

where α, β and γ are the parameters which was determined so that the width of the proton's peak was minimum. Figure 3.15 shows $F_{E\Delta E}$ distribution for the (π^+, K^+) events.

Decay pions from Λ and Λ hypernuclei have a negative charge. They are absorbed into the nucleus before decaying to μ^-. The π absorption is followed the release of their mass energy, and deposit a large fraction of the energy. This makes the resolution of the particle identification worse. In figure 3.15, the distributions of $F_{E\Delta E}$ function in the two E_d region are shown. The pion peak is shifted toward the proton peak in high E_d events. For those events, we used range instead of total energy to identify the particles.

The release energy following the π absorption concentrates around stop point of the incident π, since the emitted protons or nuclei have short range due to their small energy. Thus the range reflects the incident energy better than the measured pulse height. Figures 3.16 show the separation using the range(R) and the ΔE. PI function by $R - \Delta E$ method($F_{R\Delta E}$) was defined in same manner with the $E - \Delta E$ method as

$$F_{R\Delta E} \equiv F_{R\Delta E}(R, \Delta E) = \alpha \log R + \beta \log \Delta E + \gamma. \tag{3.14}$$

In the higher energy region the $F_{R\Delta E}$ gives better resolution of particle identification than the $F_{E\Delta E}$. On the other hand, in the lower energy region, $F_{R\Delta E}$ is not so effective due to the lack of the collection efficiency of scintillation photon in the multi-anode phototube.

We set the particle windows in the PI functions to obtain the yield of decay pions and protons as in Table 3.1. The low energy protons from nonmesonic decay are considered to be die to the intranuclear collisions, in other word the final state interaction. These protons modified the measured energy and angular distributions from those at the stage of nonmesonic decay occurred. Therefore the energy threshold for the protons was set higher than the sensitivity of our decay counter systems.

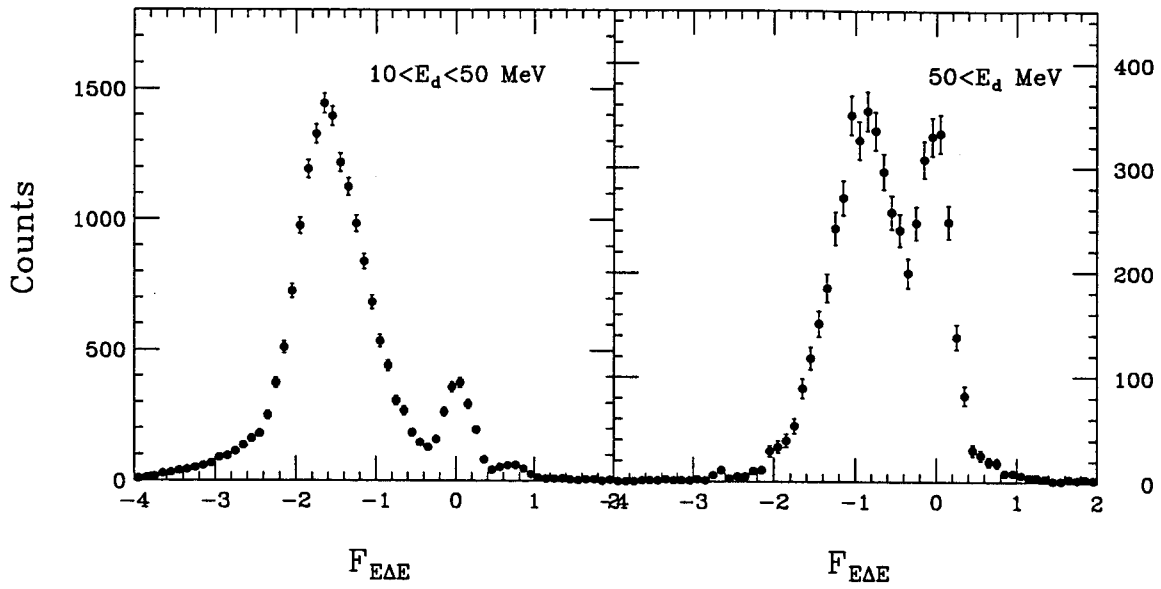

Figure 3.15: PI function($F_{E\Delta E}$) for decay particles whose energies(E_d) are in $10 < E_d < 50$ MeV(left) and in $E_d > 50$ MeV(right).

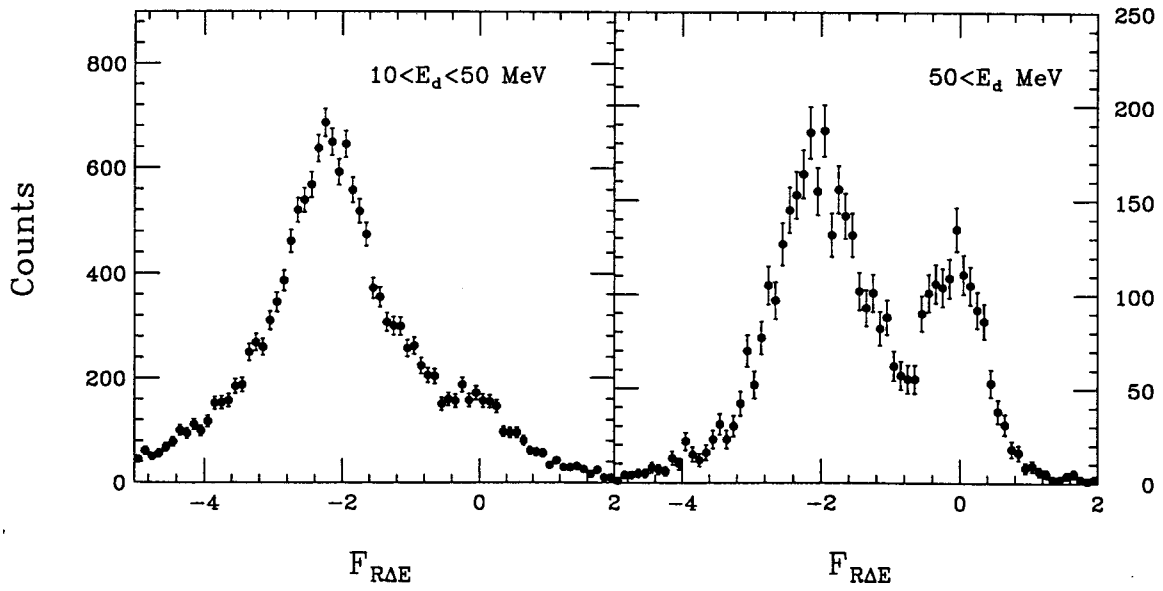

Figure 3.16: PI function($F_{R\Delta E}$ for decay particles whose energies(E_d) are in $10 < E_d < 50$ MeV(left) and in $E_d > 50$ MeV(right).

Window	Cut on PI function	Cut on Total Energy(MeV)
proton window	$-0.4 < F_{E\Delta E} < 0.5$	$30 < E_d < 50$
	$-0.8 < F_{R\Delta E}$	$50 < E_d$
pion window	$-4.0 < F_{E\Delta E} < -0.4$	$10 < E_d < 50$
	$F_{R\Delta E} < -0.8$	$50 < E_d$

Table 3.1: Definition of particle window in PI function.

Methods	E_d (MeV)	c_p (%)	c_π (%)
$E-\Delta E$	$10 < E_d < 50$	0.86	1.20
	$30 < E_d < 50$	1.05	2.57
$R-\Delta E$	$50 < E_d$	3.61	5.08

Table 3.2: The leakage factors c_p and c_π obtained by two gaussian fitting on measured distribution of PI function.

3.5.4 Resolution of particle identification

To discuss the resolution of the particle identification, we evaluated the fractions of leakage from the proton window to the pion window, or vice versa. Table 3.2 summarizes such quantities derived by fitting the PI functions with two gaussian in certain energy regions(Figures 3.17, 3.18). For the $F_{E\Delta E}$ the pion peak has the tail in higher value side. This is due to the pion absorption. In order to take it into account, the gaussian which has different width in lower and higher side was used to fit the pion peak. The factor $c_p(c_\pi)$ is defined as the ratio of protons(pions) in the π(p) window to those in the p(π) window.

The number of events observed in the windows(N_p^{obs}, N_π^{obs}) are expressed in terms of the net contribution of protons or pions in the windows as

$$\begin{pmatrix} N_p^{obs} \\ N_\pi^{obs} \end{pmatrix} = \begin{pmatrix} 1 & c_\pi \\ c_p & 1 \end{pmatrix} \begin{pmatrix} N_p \\ N_\pi \end{pmatrix}. \tag{3.15}$$

After the calculations, one can derive the formula applicable to evaluations of the asymmetry as

$$\begin{aligned} A_p &= \frac{N_p^{obs}A_p^{obs} - c_\pi N_\pi^{obs}A_\pi^{obs}}{N_p^{obs} - c_\pi N_\pi^{obs}}, \\ A_\pi &= \frac{N_\pi^{obs}A_\pi^{obs} - c_p N_p^{obs}A_p^{obs}}{N_\pi^{obs} - c_p N_p^{obs}}, \end{aligned} \tag{3.16}$$

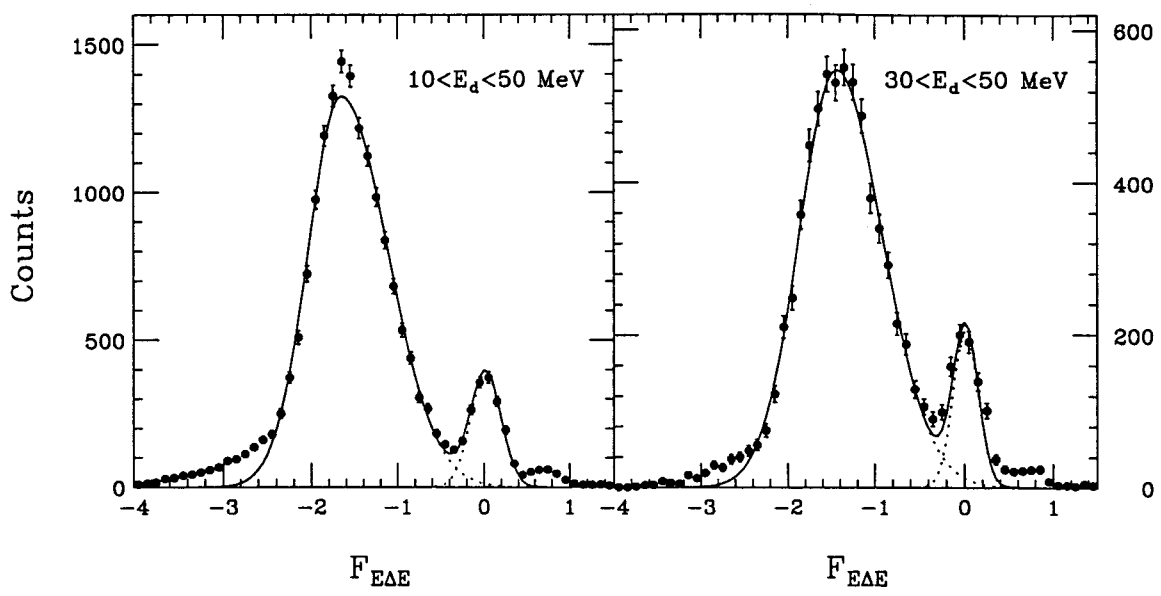

Figure 3.17: PI functions($F_{E\Delta E}$) fitted by two gaussian to evaluate the fraction of leakage from the proton window to the pion window, or vice versa. The energy of the decay particles are in the region $10 < E_d < 50$(left) and $30 < E_d < 50$(right).

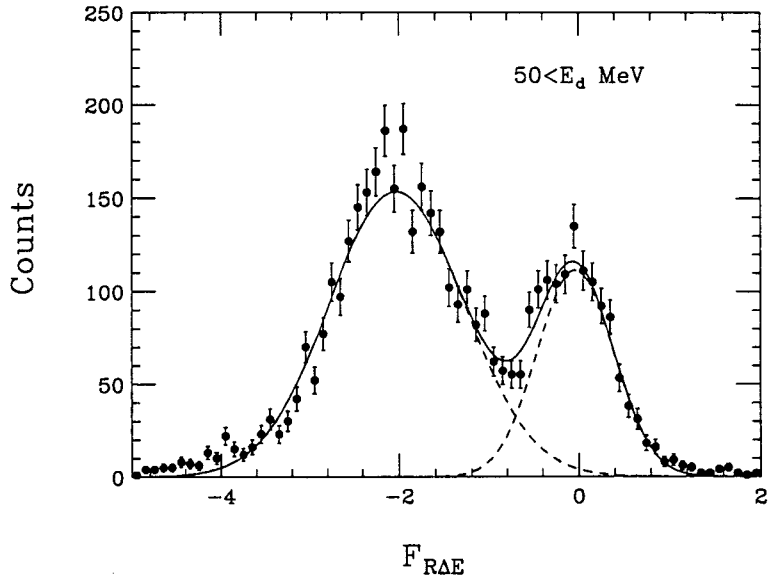

Figure 3.18: Same as Figure 3.17 for $F_{R\Delta E}$. The energy of the decay particles are in the region $50 < E_d$.

where $A_p(A_\pi)$ and $A_p^{obs}(A_\pi^{obs})$ are "net" and "observed" up/down asymmetry($Y_{up} - Y_{down}/Y_{up}+Y_{down}$) of the decay particles. The second order of c_p and c_π are included.

Chapter 4

Results

The $(\pi^+, \pi^{+\prime}X)$ events were analyzed to study the instrumental asymmetry of the decay counter systems. The instrumental asymmetry in the present decay counter systems is shown to be small. The rest of this chapter is devoted to the production of hypernuclei by the ^{6}Li(π^+, K^+) reaction and their asymmetric weak decay.

4.1 $(\pi^+, \pi^{+\prime}X)$ reaction

The asymmetries(A) of the decay particles are derived from the ratio(R) of the yield on upper and lower counter systems as

$$R = \frac{Y_{Upper}(-)}{Y_{Lower}(-)} \frac{Y_{Lower}(+)}{Y_{Upper}(+)} = \left(\frac{1-A}{1+A}\right)^2, \tag{4.1}$$

where $Y_{Upper(Lower)}(\pm)$ stands for the yield of the upper(lower) counter systems at the positive(negative) scattering angle in the horizontal plane. To reduce systematic errors, we took the (π^+, K^+) data at the positive and negative scattering angle simultaneously. The direction of the polarization is determined by the scattering angle of the reaction. In our notation the scattering angle defined as the direction of the polarization is upward at the positive scattering angle. Then the ratio(R) cancels out the spurious asymmetries which are, for example, caused by

- difference of the acceptances of the upper and lower counter systems,
- misalignment of the beamline, the target and the decay counter systems,
- difference of the acceptance of the scattered particle spectrometer for the positive/negative scattering angle.

To monitor how this cancellation works, we analyzed the $(\pi^+, \pi^{+\prime}X)$ data which was taken in the normal (π^+, K^+) run simultaneously.

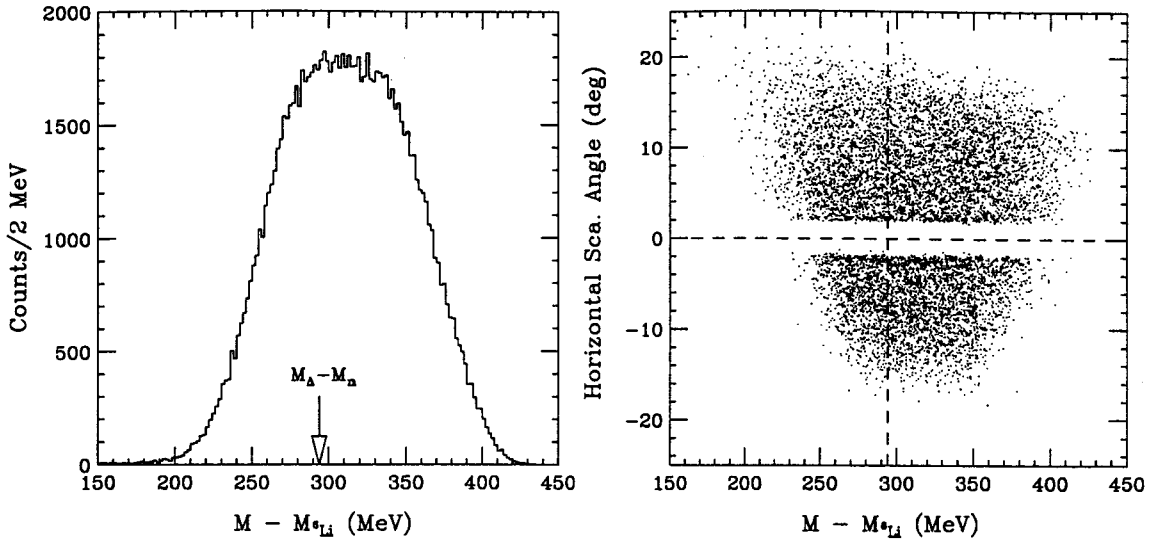

Figure 4.1: Missing mass spectrum of the $(\pi^+, \pi^{+\prime}X)$ reaction.

	Horizontal Scattering Angle	Y_{Upper}/Y_{Lower}		$\sqrt{R}$	$A^{obs} \pm \Delta A^{obs}_{stat}$
		$\theta_K < 0$	$\theta_K > 0$		
Proton	$2 < \lvert\theta_K\rvert < 7°$	433/496	390/440	0.992	0.004 ± 0.024
	$7 < \lvert\theta_K\rvert < 15°$	425/477	475/524	0.991	0.004 ± 0.023
Pion	$2 < \lvert\theta_K\rvert < 7°$	1298/1457	1123/1246	0.994	0.003 ± 0.014
	$7 < \lvert\theta_K\rvert < 15°$	1284/1372	1456/1500	0.982	0.009 ± 0.013

Table 4.1: Asymmetry of decay particles from the $(\pi^+, \pi^{+\prime}X)$ events.

The missing mass spectrum of the $(\pi^+, \pi^{+\prime})$ reaction is shown in Figure 4.1. Since the momentum acceptance of SKS spectrometer has only $\pm 10\%$, the shape of the spectrum is determined by the acceptance. The central momentum of the spectrometer is about 700 MeV/c, which corresponds to Δ production on nucleus. Thus the most of the $(\pi^+, \pi^{+\prime}X)$ events come from the Δ production followed the pions and protons emitting from Δ decay. Such pions and protons are expected to have no up/down asymmetry, since there is no weak interaction involved in the reaction. Therefore the analysis of the $(\pi^+, \pi^{+\prime}X)$ events provides the information on the spurious asymmetry of the decay counter systems.

Table 4.1 shows the pion and proton asymmetries by the $(\pi^+, \pi^{+\prime}X)$ reaction in two horizontal-scattering angle regions. We introduced the excitation energy(E_X^{PIK}) which was evaluated from the momenta of the beam and the scattered pion and the

scattering angle under the kinematics of the(π^+, K^+) reaction. To monitor the asymmetries in same acceptance of the spectrometer with the ground state region of the (π^+, K^+) reaction, we used the events whose E_X^{PIK} were in the region of $-20 < E_X^{PIK} < 20$ MeV. The errors for the asymmetries, ΔA_{stat}^{obs}, were estimated from the statistics. The instrumental asymmetry was found to be at most 1% in each case and thus the cancellation works well.

4.2 Excitation energy spectrum

The single spectrum of the excitation energy in the ^{6}Li(π^+, K^+) reaction is shown in Figure 4.2(top). The ground state of $^6_\Lambda$Li is clearly seen in the spectrum. Because of the large momentum transfer, the dominant part of the cross section of the reaction goes to the highly excitation energy region, which is characterized by the so-called quasifree(QF) Λ production.

Middle and bottom spectra in Figure 4.2 are that in coincidence with decay pions and decay protons, respectively. In the proton gated spectra, the ground state and s-substitutional state($E_X \sim 20$ MeV) are enhanced because the energetic proton can be emitted only by the nonmesonic decay of the hypernuclei. The protons from the mesonic decay cannot be detected by our decay counter systems because of its low energy($\sim$ 5 MeV). The protons from the decay of Λ produced by the QF process might have large energy, however the decay counter systems have no acceptance for such protons boosted forward by the Λ momentum. On the contrary, the p-substitutional state is strongly suppressed in the proton gated spectrum, because the state is above the Λ emitting threshold.

One of the advantage of using the (π^+, K^+) reaction is that the reaction produced hypernuclei in the ground state more than the p- or s-substitutional state. In the previous (K^-, π^-) experiment at BNL the ground state of $^6_\Lambda$Li was hardly seen in the pion gated spectrum(see Figure 1.5). On the other hand, in the present experiment the ground state is well separated from the substitutional states. It is important to determine the polarization of the produced hypernuclei as mention in Section 1.5.

4.3 Asymmetry of decay particles

Table 4.2 shows the yields of the decay protons and the decay pions in the ground state region of $^6_\Lambda$Li($-4 < E_X < 4$ MeV). Here "Upper" and "Lower" are the location of the decay counter systems, and θ_K stands for the horizontal scattering angle of the

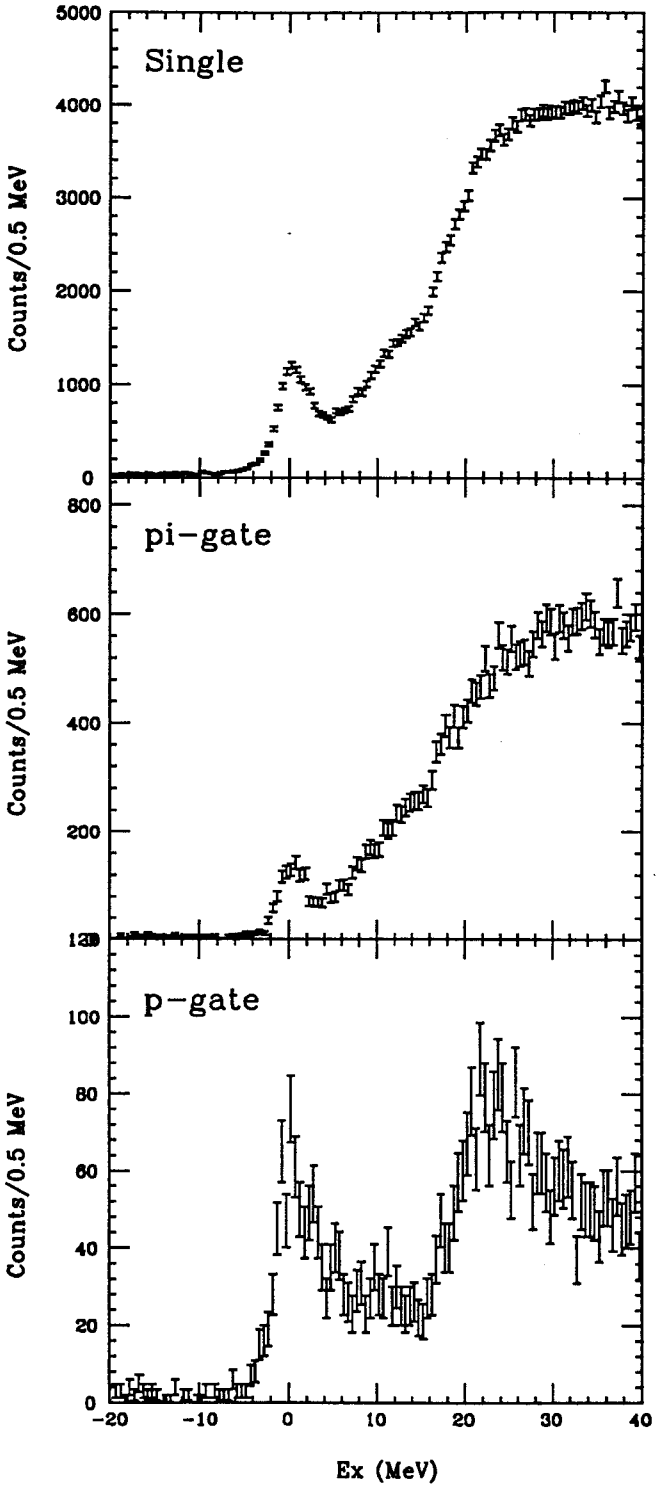

Figure 4.2: Excitation energy spectra of ${}^{6}_{\Lambda}$Li are shown. Middle and bottom are the spectra in coincidence with decay pions and decay protons.

	Horizontal Scattering Angle	Y_{Upper}/Y_{Lower}		$\sqrt{R}$	$A^{obs} \pm \Delta A^{obs}_{stat}$
		$\theta_K < 0$	$\theta_K > 0$		
Proton	$2 < \lvert\theta_K\rvert < 7°$	72.2/86.8	80.0/70.8	0.858	0.08 ± 0.06
	$7 < \lvert\theta_K\rvert < 15°$	42.8/48.6	48.2/49.2	0.948	0.03 ± 0.08
Pion	$2 < \lvert\theta_K\rvert < 7°$	169.2/144.6	127.4/179.8	1.285	-0.13 ± 0.04
	$7 < \lvert\theta_K\rvert < 15°$	139.0/87.4	101.4/143.6	1.501	-0.20 ± 0.05

Table 4.2: Asymmetries of decay particles in the ground state region of ${}^{6}_{\Lambda}$Li.

	Horizontal Scattering Angle	$A^{obs} \pm \Delta A^{obs}_{stat} \pm \Delta A^{obs}_{sys}$
Proton	$2 < \lvert\theta_K\rvert < 7°$	$0.10 \pm 0.07 \pm 0.01$
	$7 < \lvert\theta_K\rvert < 15°$	$0.04 \pm 0.10 \pm 0.01$
Pion	$2 < \lvert\theta_K\rvert < 7°$	$-0.16 \pm 0.05 \pm 0.01$
	$7 < \lvert\theta_K\rvert < 15°$	$-0.25 \pm 0.06 \pm 0.01$

Table 4.3: The asymmetries of decay particles with the corrections(see text).

(π^+, K^+) reaction. R and A^{obs} are defined in Eq. 4.1. The continuous backgrounds in the excitation spectra are already subtracted in the table.

Systematic errors for the observed asymmetries were monitored by ^{6}Li$(\pi^+, \pi^{+\prime}X)$ reaction and were evaluated to be less than 1% for both the pion and proton(see Sec. 4.1). To obtain real asymmetries, the following corrections have to be applied.

- The misidentification of decay particles can modify the measured asymmetries. In terms of the leakage into the PI window, discussed in Sec. 3.5.4, the measured asymmetries can be corrected by Eq. 3.16.
- The measured asymmetries are attenuated due to the finite acceptance of the decay counter systems. This attenuation factor was estimated by a Monte Carlo simulation including the geometrical configuration, the efficiencies and the resolutions of the counter elements. The simulation shows that the attenuation factor of the asymmetry is 0.804.

The asymmetries with these corrections are shown in Table 4.3.

Horizontal Scattering Angle	P_Λ
$2 < \|\theta_K\| < 7°$	$0.25 \pm 0.08^{+0.03}_{-0.02}$
$7 < \|\theta_K\| < 15°$	$0.39 \pm 0.09 \pm 0.02$

Table 4.4: The polarization of Λ in the ${}^{5}_{\Lambda}$He determined by the measured asymmetries of mesonic decay.

4.4 Polarization of ${}^{5}_{\Lambda}$He

The polarization(P_Λ) of Λ in the ${}^{5}_{\Lambda}$He can be derived by the asymmetry of the mesonic decay(A_π) with the asymmetry parameter(α_π-) as

$$A_\pi = \alpha_\pi - P_\Lambda. \tag{4.2}$$

In order to determine the polarization experimentally, we applied the asymmetry parameter for the free Λ decay($\alpha_{\pi^-}^{free} = 0.642 \pm 0.013$) as that for the mesonic decay. Table 4.4 shows the polarizations in two horizontal-scattering angle regions. The quasifree events and the higher excited states of ${}^{6}_{\Lambda}$Li might be in the ground state region due to the excitation energy resolution. The contribution to the asymmetries was estimated by that in the higher excitation energy region and was taken into account as systematic errors.

4.5 Asymmetry of nonmesonic decay of ${}^{5}_{\Lambda}$He

The nuclear effects on the initial and the final state of the nonmesonic decay can modify the measured asymmetry from the asymmetry for two-body ΛN weak interaction. These nuclear effects are due to the Fermi momentum of Λ and the rescattering of emitted nucleons The effects tend to decrease the asymmetry. The Monte Carlo simulation was employed to evaluate the attenuation due to the nuclear effects within the same framework in Appendix of Ref. [8].

Figure 4.3 shows the energy spectra of the proton from proton- and neutron-stimulated nonmesonic decay of ${}^{5}_{\Lambda}$He. Here the evaporation process was ignored since the residual nucleus has only three nucleons and the low energy proton from the process cannot be detected our decay counter system. The gross shape of the spectrum for $\Lambda p \rightarrow np$ decay is determined by the Fermi momenta of initial Λ and proton. The dashed lines in the figure represent the protons emitted by the

Horizontal Scattering Angle	A_p/k
$2 < \|\theta_K\| < 7°$	$0.11 \pm 0.08 \pm 0.01$
$7 < \|\theta_K\| < 15°$	$0.05 \pm 0.10 \pm 0.01$

Table 4.5: The asymmetries of the nonmesonic decay of the ${}^{5}_{\Lambda}$He. k represents the attenuation factor due to the nuclear effects in the initial and the final state of the nonmesonic decay.

scattering between decay products and nucleons in nucleus. It is important to know how much these protons were counted into the observed asymmetries, since the attenuation is mainly due to such kind of protons.

GEANT simulation for the decay counter system was carried out with the obtained energy spectra of protons above. The ratio of the proton- to the neutron-stimulated nonmesonic decay was assumed as unity. Figure 4.4(left) shows the result of the simulation. The histogram represents the sum of the total energy deposits on SSD, RSC and CTC. Because the energy deposits on the target and DH was not measured, the measured energy was smaller than the original energy(E_p). The distribution of the original energy is shown in Figure 4.4(right) where the entries were gated by the experimental threshold, 30 MeV. The effective threshold energy was about 50 MeV. The plot in the figure represents the measured energy spectra in the ground state region of the (π^+, K^+) reaction. The counts of the simulation are normalized by the number of the protons whose energies were above 10 MeV.

The dashed lines in the figures are the contribution of the protons which is scattered by nuclear cascade process before escaping from nucleus. The present energy threshold eliminated almost of such protons, however there was still a finite fraction of it. Same analysis with that for the experimental data turned out that the attenuation factor was 0.935. Table 4.5 shows the asymmetries A_p/k in the two horizontal-scattering angle regions.

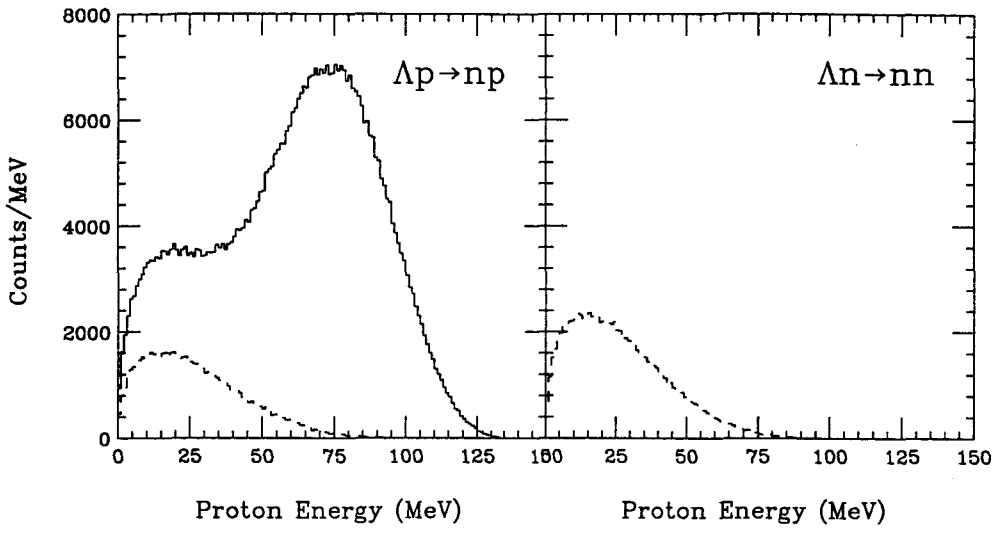

Figure 4.3: Proton energy spectra from the (left)proton- and (right)neutron-stimulated nonmesonic decay of ${}^{5}_{\Lambda}$He generated by a Monte Carlo simulation. Dashed lines present the spectra of the scattered proton in the nuclear cascade process. In the simulation a half million decays are generated for each decay modes.

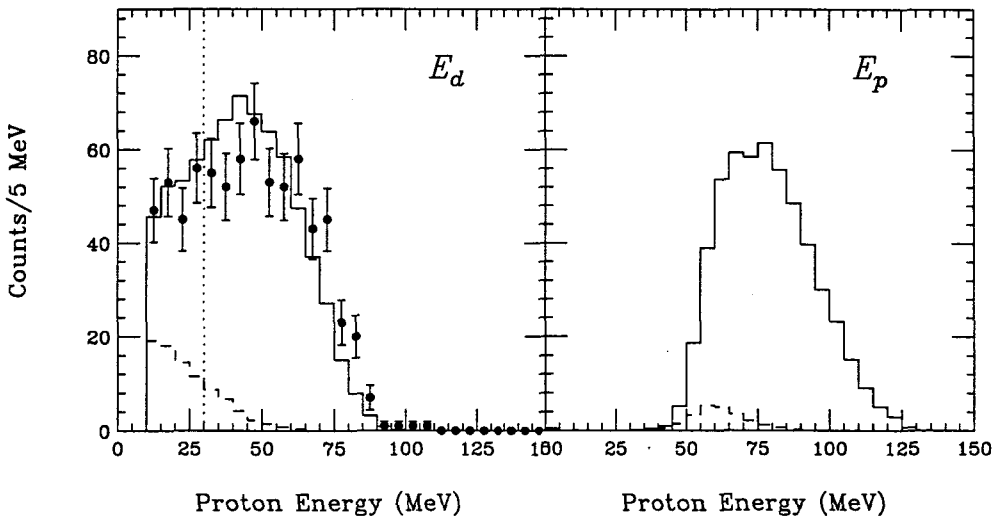

Figure 4.4: Measured proton energy spectrum is shown(left). The plot is obtained from the experimental data and the histogram is the GEANT simulation. Right histogram presents the energy which the proton has originally. The experimental threshold, 30 MeV, corresponds to the 'original' energy of about 50 MeV.

Chapter 5

Discussions

5.1 Polarization

The cross section and polarization have been calculated for the ^{6}Li(π^+, K^+) reaction at 1.05 GeV/c[31]. In the calculation, DWIA calculation was applied on the basis of the elementary amplitudes for the (π^+, K^+) reaction, which include both spin-flip and spin-nonflip amplitudes. For the initial nuclear and final hypernuclear wave functions the Cohen-Kurath model was employed. The calculation is summarized in Table 5.1. The main component of the ground state is the 2_1^- state of the doublet which has $(p_{3/2})_p(s_{1/2})_\Lambda$ configuration mainly. The 1_{gs}^- partner has smaller cross section because the state is excited dominantly through the spin-flip interaction.

In general, particle decays of hypernucleus reduce its polarization[28]. In the case of the 2_1^- state of the $^6_\Lambda$Li, a proton is emitted with a $p_{3/2}$ partial wave. Such a stretched transition does not modify the polarization. On the other hand, the polarization of the 1_1^- has opposite direction to that of 2_1^- state. The depolarization factors for the proton emission of the 1_1^- state is -0.5. Therefore the final polarization of $^5_\Lambda$He has same direction with the 2_1^- state. This is naturally understood because the spin polarization of Λ has same direction for the 2_1^- and the 1_1^- states.

There are the 1_2^- and 0^- doublet around the ^{5}Li + p threshold. These sates has $(p_{1/2})_p(s_{1/2})_\Lambda$ configuration mainly. The calculation predicted the excitation energies of the states around 6 MeV. The excitation energies, however, depend on the models in the calculation, and they could be around 4 MeV. The $^5_\Lambda$He polarization of the states is small as $0.03(\theta{=}6°)$–$0.05(14°)$. Therefore, if the ground state can not be separated from the 1_2^- and 0^- doublet due to the finite excitation energy resolution, the measured polarization is reduced because of the small polarization of the doublet. Table 5.1 shows the averaged polarization in two cases, one is for the ground state

state($^{6}_{\Lambda}$Li)		$\theta = 6°$	$\theta = 10°$	$\theta = 14°$	$\theta = 18°$
1^-_{gs}	$\frac{d\sigma}{d\Omega}[\mu b/sr]$	0.78	0.71	0.55	0.34
	P	−0.443	−0.566	−0.590	−0.570
	$P(^{5}_{\Lambda}He)$	0.222	0.283	0.295	0.285
2^-_1 (0.42 MeV)	$\frac{d\sigma}{d\Omega}[\mu b/sr]$	6.90	5.17	3.23	1.64
	P	0.249	0.385	0.490	0.568
	$P(^{5}_{\Lambda}He)$	0.249	0.385	0.490	0.568
1^-_2 (6.12 MeV)	$\frac{d\sigma}{d\Omega}[\mu b/sr]$	0.97	0.90	0.70	0.44
	P	0.127	0.159	0.163	0.154
	$P(^{5}_{\Lambda}He)$	0.127	0.159	0.163	0.154
0^-_1 (6.18 MeV)	$\frac{d\sigma}{d\Omega}[\mu b/sr]$	3.43	2.44	1.44	0.68
	P	–	–	–	–
$1^-_{gs} + 2^-_1$	$\frac{d\sigma}{d\Omega}[\mu b/sr]$	7.68	5.88	3.78	1.98
	$P(^{5}_{\Lambda}He)$	0.246	0.373	0.462	0.519
all	$\frac{d\sigma}{d\Omega}[\mu b/sr]$	12.08	9.22	5.92	3.10
	$P(^{5}_{\Lambda}He)$	0.167	0.253	0.314	0.354

Table 5.1: Calculated cross section($d\sigma/d\Omega$) and polarization(P) of low-lying $^{6}_{\Lambda}$Li hypernuclear state are shown. $P(^{5}_{\Lambda}He)$ represents the polarization of $^{5}_{\Lambda}$He after proton emission.

Scattering angle	P_{cal}		P_{exp}
	$1^-_{gs} + 2^-_1$	all	
$2 < \theta_K < 7°$	0.181	0.123	$0.25 \pm 0.08^{+0.03}_{-0.02}$
$7 < \theta_K < 15°$	0.368	0.250	$0.39 \pm 0.09 \pm 0.02$

Table 5.2: Polarization folded by the SKS acceptance(P_{cal}) and that measured in the present experiment(P_{exp}) are shown.

doublet only and the other is for four states all.

In the experiment, the polarization is derived from the up/down asymmetry of the $^{5}_{\Lambda}$He mesonic decay. The measured polarization reflects that in the vertical direction. The calculated polarization is defined along the axis perpendicular to the plane of the (π^+, K^+) reaction. Since the present spectrometer, SKS, has a finite vertical acceptance, the direction of the polarization could be tilted and the measured polarization is therefore reduced. The calculated polarization was folded by the SKS

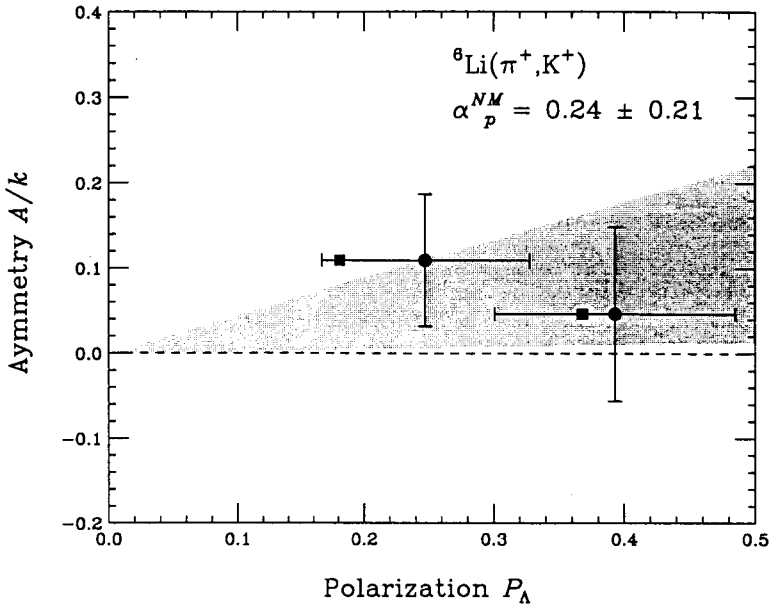

Figure 5.1: The observed asymmetries $A/k \equiv \alpha_p P_\Lambda$ as a function of polarization of Λ. Squares are indicate the calculated polarization.[31]

acceptance as shown in Table 5.2. The present values are quite consistent with the calculation. The experiment prefers the polarization averaged over the ground state doublet only. This implies that the second doublet is highly excited so that the contribution of the doublet cannot seen in the ground state region($-4<E_X<4$ MeV), where the experimental resolution of the excitation energy is 4.2 MeV(FWHM).

5.2 Asymmetry of nonmesonic decay

The present results are summarized in Figure 5.1. The circles are indicates the asymmetries of the nonmesonic decay and the polarization which derived by the asymmetries of the mesonic decay. The theoretical calculation for the polarization is indicated by the squares.

The intrinsic asymmetry parameter(α_p^{NM}) is useful to discuss the asymmetry of nonmesonic decay. It is defined from Eq. 1.9 as

$$\begin{aligned} A_p/k \equiv \frac{W(\pi) - W(0)}{W(\pi) + W(0)} &= \alpha_p^{NM} P_\Lambda, \\ \alpha_p^{NM} &= A_p/k/P_\Lambda. \end{aligned} \tag{5.1}$$

Then the weighted mean of α_p^{NM} between two data points gives $\alpha_p^{NM} = 0.24 \pm 0.21$ for the ${}^{5}_{\Lambda}$He, as shown in Figure 5.1 by shaded region.

5.2.1 Comparison to other experiments

The present result, positive and relatively small asymmetry, indicates that either the final isospin $I_f = 0$ amplitude(c, d) or $I_f = 1$ amplitude(f) is small, and the relative phase of these amplitudes are same. As discussed in Sec. 1.2, the ratio of the neutron- to proton-stimulated decay(Γ_n/Γ_p) is sensitive to the isospin structure of the decay mechanism. Experimental value of $\Gamma_n/\Gamma_p \sim 1$ indicates dominance of $I_f = 1$ amplitude and minor contribution of the $I_f = 0$ amplitude to the decay rate, since the final neutron-neutron system is permitted to have final isospin 0. Another possibility of the smallness is the large contribution of the initial ${}^1S_0$ amplitudes(a, b), although the phenomelogical analysis for 4- and 5-body hypernuclei predicted small. Both the a and b amplitudes have final isospin 1 therefore the existing Γ_n/Γ_p do not contradict also in this case.

The asymmetry parameter for p-shell hypernuclei has opposite sign of the present result. The p-wave contribution in initial ΛN system possibly changes the asymmetry.

5.2.2 Comparison to calculations

In the one pion exchange model, the calculated asymmetry is $-0.2 \sim -0.4$[48, 13] depend on the model. The magnitude is consistent but the sign is opposite with the present results. Large contribution of ${}^3S_1 \rightarrow {}^3D_1$ amplitude(d) and relative opposite sign between ${}^3S_1 \rightarrow {}^3P_1$ amplitude(f). Once the heavier mesons such as ρ, K, K^*, η and ω are included, the calculated value is changed 30%[13]. However the experiment can not be explained, rather the discrepancy is increased. The contributions of heavy mesons cancel among each other, therefore they can not modify the large amplitude of pion exchange so much. Same things happen on the branching ratio Γ_n/Γ_p. The calculation estimates about 0.1 but the experiments lies around unity. This is again due to the large contribution of amplitudes d, whose final isospin is 0.

There is another approach to the nonmesonic decay, that is the model based on direct quark exchange[16]. In this model, the interaction at short distance is described by a direct quark mechanism and superposes on one-pion exchange as a long range interaction. The calculation provides the range $0.20 \sim -0.44$ and $0.12 \sim 0.79$ for the asymmetry parameter and the branching ratio, respectively. The limits of the

ranges correspond to the sums of two interactions, direct quark and pion exchange, with relative phase is positive and negative. The obtained asymmetry prefers positive case, while the branching ratio prefers negative case. Although the model is still in the developing stage, there is some interesting feature, which is the large contribution of $\Delta I = 3/2$ amplitudes for initial $^1S_0$ state and the large amplitudes for final isospin 1 even if the $\Delta I = 1/2$ only case. This might be a possibility to solve the consistency between theory and experiment on the nonmesonic decay phenomenon.

5.2.3 Future Prospect

In this thesis, only the asymmetry of weak decay has been reported. In the experiment, we accumulated about 600 and 1100 events in coincidence of decay pions and protons in ground state region. This statistics is 4 times of the previous BNL experiment. Our data can revise, for example, the existing Γ_n/Γ_p ratio(0.87 ± 0.37[7]) with better precision.

Currently the experiment to study the inverse process pn$\rightarrow$ pΛ is under preparation at RCNP[49]. The analyzing power of the reaction cross section with longitudinally polarized proton beam gives the interference of parity conserving and parity violating amplitude. It is the same quantity as the asymmetry of the nonmesonic decay of hypernuclei. Large polarization of proton beam as $\sim$0.8 and careful design of detector system to overcome the huge background from the strong interaction should allow direct study of weak baryon-baryon interaction. It can be solve the problem on the nonmesonic decay.

The present experiment demonstrated the asymmetry of π^- mesonic decay with respect to the polarization of the $^5_\Lambda$He hypernucleus. The angular distribution of π^- depends on the initial and final spin-parity state of hypernucleus. Accordingly it opens a new field of hypernuclear spectroscopy with high intensity pion beam such as the JHF project in the near future.

Chapter 6

Conclusion

- The experiment, KEK-PS E278, to measure the asymmetric weak decay of ${}^{5}_{\Lambda}$He was carried out at the K6 beamline of 12 GeV proton synchrotron in KEK. The ^{6}Li(π^+, K^+) reaction at P_π=1.05 GeV/c was used to produce polarized ${}^{6}_{\Lambda}$Li which decays into ${}^{5}_{\Lambda}$He with emitting proton. The momentum of scattered kaons were measured by the SKS spectrometer which was developed by the collaboration of INS and KEK for previous experiment, E140a. The SKS covered the scattering angle from -18 to 18 degrees enough to introduce polarization in the Λ hypernucleus. We newly installed the decay counter systems above and below the target in order to measure the up/down asymmetry of decay products.

- The analysis of $(\pi^+, \pi^{+\prime}X)$ data, which was taken in normal (π^+, K^+) run simultaneously, shows the systematic error for the measured asymmetry was less than 1% for both pion and proton. The simultaneous measurement of positive and negative scattering angle canceled out the spurious asymmetry caused by the difference of the efficiency of decay counter systems, that of the acceptance of the SKS spectrometer in positive and negative scattering angle and the misalignment of our apparatus.

- In the excitation energy spectrum of ${}^{6}_{\Lambda}$Li, we can clearly see the ground state peak where the ${}^{5}_{\Lambda}$He is produced exclusively. This is the advantage of using the (π^+, K^+) reaction. The large momentum transfer populates the ground state more than the p- or s-substitutional state. Also in the spectrum gated by decay pion, the ground state is well separated from quasifree events and highly excited states. It is important to determine the polarization of the produced hypernucleus, because the polarization derived by the asymmetry of

decay pions.

- The polarization of the ${}^{5}_{\Lambda}$He was derived by the measured pion asymmetry. Obtained values are $P_\Lambda = 0.25 \pm 0.08^{+0.03}_{-0.02}$, $0.39 \pm 0.09 \pm 0.02$ averaged in the two scattering angle region, $\theta_K = 2 \sim 7$, $7 \sim 15$ degrees, respectively. The polarized hypernuclei was really produced and the polarization was consistent with DWIA calculation based on the elementary amplitudes for the (π^+, K^+) reaction.

- The asymmetry of the proton from the nonmesonic decay of ${}^{5}_{\Lambda}$He was measured as $A_p/k = 0.11\pm0.08\pm0.01$, $0.05\pm0.10\pm0.01$ in the two scattering angle region. The results shows the asymmetry parameter for nonmesonic decay is $\alpha_p^{NM} = 0.24\pm0.21$, which is small and has opposite sign with comparing to the previous p-shell hypernuclei experiment. Combining with existing experimental data of the branching ratio, final isospin I_f=1 amplitudes are dominant and the phase of I_f=1 and 0 amplitudes are same. While the meson exchange model predict the dominance of I_f=0 amplitudes due to the strong tensor force in pion exchange potential and the phase of these amplitudes are relatively opposite to the I_f=1 amplitudes. There is no theoretical calculation agreed with the present asymmetry parameter as well as the branching ratio.

- We have four times decay events comparing with the previous BNL experiment. Although the analysis for π^0 detectors has not been done yet, it is promising to provide the branching ratio Γ_n/Γ_p with better precision.

- The present experiment demonstrated the asymmetry of π^- mesonic decay with respect to the polarization of the ${}^{5}_{\Lambda}$He hypernucleus. The angular distribution of π^- depends on the initial and final spin-parity state of hypernucleus. Accordingly it opens a new field of hypernuclear spectroscopy with high intensity pion beam such as the JHF project in the near future.

- The experiment to study inverse process pn$\rightarrow$ pΛ is under preparation at RCNP. The analyzing power of the reaction cross section with longitudinally polarized proton beam gives the interference of parity conserving and parity violating amplitude. It is the same quantity as the asymmetry of the nonmesonic decay of hypernuclei. The experiment should allow direct study of weak baryon-baryon interaction. It can be solve the problem on the nonmesonic decay.

Acknowledgements

The author would like to express his sincere gratitude to Professor T. Kishimoto, who was the spokesman of the present experiment(KEK-PS E278), for his valuable suggestions and discussions. He made vigorous efforts throughout the experiment. This work would not completed without his encouragement.

The author would like to express his sincere gratitude to Professor H. Ejiri for guiding and encouraging the author since his entrance of graduated school.

The author would like to express his best regards to all the collaborators of the experiment, Prof. H. Bhang, Dr. T. Hasegawa, Prof. O. Hashimoto, Mr. K. Ikeda, Mr. M. Ishikawa, Dr. Y. Kim, Prof. K. Maeda, Ms. K. Manabe, Prof. T. Nagae, Prof. T. Nakano, Dr. H. Noumi, Mr. A. Okusu, Mr. H. Park, Ms. M. Sekimoto, Prof. T. Shibata, Mr. N. Shinkai, Dr. T. Takahashi, Mr. Y. Tanaka and Dr. M. Youn. The author owes great deal to them for their participations.

The author would like to acknowledge Professor T. Fukuda and Dr. H. Outa for their encouragement and valuable discussion.

The autor would like to give his thanks to the members of the laboratory in Osaka University, Dr. K. Fushimi, Dr. K. Nagata, Dr. N. Kudomi, Mr. K. Kume, Dr. R. Hazama. They introduced the ineteresings in the non-accelarator experiment to the author. The autor also aknowledge secretaries Ms. M. Nagata, E. Yamaguchi and E. Matsumoto for their support.

The author would like to thank Professor K. Nakai, Professor T. Ohshima, Proffesor K. Nakamura, Professor J. Chiba and Professor T.K. Ohska for supports to carry out the experiment. The author would like to also thank the accelerator and cryogenic group of KEK for their supports.

This work is partially supported by the JSPS Fellowships for Japanese Junior Scientists, the Grant-in-Aid of Scientific Research, Ministry of Education, Science and Culture.

References

[1] T. Motoba, K. Itonaga and H. Bandō, Nucl. Phys. **A489**(1988)683.

[2] H. Outa, et al., Nucl. Phys. **A585**(1995)109c.

[3] I. Kumagai-Fuse, S. Okabe and Y. Akaishi, Phys. Lett. **B345**(1995)386.

[4] M.M. Block and R.H. Dalitz, Phys. Rev. Lett. **11**(1963)96.

[5] V.J. Zeps and G.B. Franklin, *Proc. of the 23rd INS inteernational Symp. on Nuclear and Particle Physics with Meson Beams in the 1 GeV/c Region*, Mar. 1995, eds. S. Sugimoto and O. Hashimoto, Universal Academy Press, p. 227.

[6] H. Outa, et al., to be submitted.

[7] J.J. Szymanski, et al., Phys. Rev. **C43**(1991)849.

[8] H. Noumi, et al., Phys. Rev. **C52**(1995)2936.

[9] J.B. Adams, Phys. Rev. **156**(1967)1611.

[10] B.H.J. McKeller and B.F. Gibson, Phys. Rev. **C30**(1984)322.

[11] K. Takeuchi, H. Takaki and H. Bando, Prog. Theo. Phys. **73**(1985)841.

[12] J.F. Dubach, Nucl. Phys. **A450**(1986)71c.

[13] A. Parreño, A. Ramos and C. Bennhold, Phys. Rev. **C56**(1997)339.

[14] C.-Y. Cheung, D.P. Heddle and L.S. Kisslinger, Phys. Rev. **C27**(1983)335.

[15] D.P. Heddle and L.S. Kisslinger, Phys. Rev. **C33**(1986)608.

[16] T. Inoue, S. Takeuchi and M. Oka, Nucl. Phys. **A597**(1996)563.

[17] R.A. Schumacher, *Proc. of the U.S.-Japan Seminar on Properties and Interactions of Hyperons*, Oct. 1993, eds. B.F. Gibson, P.D. Barnes and K. Nakai, World Scientific, p. 85.

[18] J. Gerald, E.V. Hungerford and V. Zeps, *Letter of Intent* submitted to BNL-AGS PAC(1996).

[19] Particle Data Group, Phys. Rev. **D54**(1996)1.

[20] H. Bandō, T. Motoba and J. Žofka, Int. J. Mod. Phys. Vol. 5, No. 21(1990)4021.

[21] H. Ejiri, et al., Phys. Rev. **C36**(1987)1435.

[22] G.P. Gopal, et al., Nucl. Phys. **B119**(1977)362.

[23] H. Bandō, T. Motoba, M. Sotona and J. Žofka, Phys. Rev. **C39**(1989)587.

[24] M. Sotona and J. Žofka, Prog. Theo. Phys. **81**(1989)160.

[25] H. Ejiri, et al., KEK-PS proposal E160, KEK(1987), unpublished.

[26] S. Ajimura, et al., Phys. Lett. **B282**(1992)293.

[27] K. Itonaga, T. Motoba, O. Richter and M. Sotona, Phys. Rev. **C49**(1994)1045.

[28] H. Ejiri, T. Kishimoto and H. Noumi, Phys. Lett. **B225**(1989)35. In this reference the attenuation coefficient is given for the statistical tensor as usual. The statistical tensor of rank 1 is related to the polarization as $\rho_1(J) = \sqrt{\frac{3J}{J+1}}P(J)$. The explicit formula for the depolarization is then given by $P(J_f) = (J_i(J_i + 1) + J_f(J_f + 1) - L(L + 1))/(2J_f(J_i + 1))P(J_i)$.

[29] T. Kishimoto, et al., KEK-PS proposal E278, KEK(1992), unpublished.

[30] R. Bertini, et al., Nucl. Phys. **A368**(1981)365.

[31] T. Motoba and K. Itonaga, Nucl. Phys. **A577**(1994)293c.

[32] A. Okusu, et al., Annual Report, OULNS-1991(Osaka University) 9.

[33] K.H. Tanaka, et al., Nucl. Phys. and Meth. in Phys. Res. **A363**(1995)114.

[34] K.L. Brown, et al., CERN 80-04 (1980).

[35] T. Hasegawa, Doctor Thesis, Univ. of Tokyo, June 1994.

[36] T. Fukuda, et al., Nucl. Instrum. Meth. **A361**(1995)485.

[37] T. Shintomi, et al., IEEE Trans. Magn. MAG-25(1989)1667.

[38] T. Shintomi, et al., IEEE Trans. Magn. MAG-28(1992)585.

[39] J. Myrheim and L. Bugge, Nucl. Instrum. Meth. **160**(1979)43.

[40] T. Hasegawa, Nucl. Instrum. Meth. **A342**(1994)383.

[41] M. Kobayashi, et al., Nucl. Instrum. Meth. **A305**(1991)401.

[42] T.K. Ohska, et al., IEEE Trans. on Nucl. Sci. **33**(1986)98.

[43] ORBIT: developed by S. Morinobu and T. Ichihara.

[44] T. Hasegawa, et al., IEEE Trans. Magn. MAG-28(1992)805.

[45] R.L. Craun and D.L. Smith, Nucl. Instrum. Meth. **80**(1970)239.

[46] H. Bethe, Ann. Phys. **5**(1930)325, for further corrections on Bethe's formula, see S.P. Ahlen, Rev. Mod. Phys. **52**(1980)121.

[47] A. Higashi, Doctor thesis, Osaka University, 1991.

[48] J.F. Dubach, et al., Ann. Phys.(N.Y.) **249**(1996)146.

[49] T. Kishimoto, *Letter of Intent* submitted to RCNP B-PAC(1996).